Key Points:

- Twenty new [10]Be denudation rates of Western Southern Alps catchments are in the range 0.6–9 mm/yr, and likely >9 mm/yr for two glaciated catchments
- The proportion of catchment area at 1,500–2,000 masl is the variable that best correlates with observed denudation-rate variability
- Elevation sensitivity of denudation is most likely due to peri- and paraglacial processes that modulate the tectonic control on erosion

Author Contributions:

Conceptualization: Duna C. Roda-Boluda, Taylor F. Schildgen, Niels Hovius
Formal analysis: Duna C. Roda-Boluda, Taylor F. Schildgen
Funding acquisition: Duna C. Roda-Boluda, Taylor F. Schildgen
Investigation: Duna C. Roda-Boluda, Taylor F. Schildgen, Stefanie Tofelde, Aaron Bufe, Jeff Prancevic
Methodology: Duna C. Roda-Boluda

Elevation-Dependent Periglacial and Paraglacial Processes Modulate Tectonically-Controlled Erosion of the Western Southern Alps, New Zealand

Duna C. Roda-Boluda[1,2] , **Taylor F. Schildgen[1,3]** , **Hella Wittmann[1]** , **Stefanie Tofelde[3]** , **Aaron Bufe[1,4]** , **Jeff Prancevic[5]** , and **Niels Hovius[1,3]**

[1]GFZ German Research Centre for Geosciences, Potsdam, Germany, [2]Vrije Universiteit Amsterdam, Amsterdam, The Netherlands, [3]University of Potsdam, Potsdam, Germany, [4]Ludwig-Maximilians-Universität München, Munich, Germany, [5]United States Geological Survey, Moffett Field, CA, USA

Abstract Examining the links and potential feedbacks between tectonics and climate requires understanding the processes and variables controlling erosion. At the orogen scale, tectonics and climate are thought to be linked through the influence of mountain elevation on orographic precipitation and glaciation; the only documented erosional processes capable of balancing rapid rock-uplift rates are glacial erosion or coupled river incision and landsliding. Our 20 new [10]Be derived catchment-averaged denudation rates from the Western Southern Alps of New Zealand generally range between 0.6 and 9 mm/yr, within the same order of magnitude as fault-throw rates, exhumation rates, and erosion rates estimated from suspended sediment yields and landslide inventories. Combining our data with previously published [10]Be denudation rates, we find that the proportion of catchment area in the 1,500–2,000 m elevation window is the variable that best explains denudation rate variability and the disparity between rock-uplift rates and denudation rates. This correlation indicates that enhanced erosion likely occurs at 1,500–2,000 m above sea level, where periglacial and paraglacial processes have been proposed to be most active. We find that these temperature-controlled erosional processes, which are also elevation-dependent, can play a greater role in modulating erosion during interglacials than precipitation or glaciation. Our data suggest that temperature-controlled peri- and paraglacial erosion could be efficient enough to balance some of the fastest rock-uplift rates on Earth. Hence, temperature-controlled erosion could contribute to limiting orogen elevations and modulating the erosion rates dictated by rock-uplift, playing an essential role in linking tectonics and climate.

Plain Language Summary The shape and evolution of the Earth Surface depend on how the tectonic forces that build up mountains interact with the processes that wear them down through erosion. These erosional processes are often regulated by climate; for example, erosion is commonly more efficient where there are glaciers or in the wetter side of mountain ranges. We present 20 new [10]Be concentrations, which are commonly used as a proxy for how fast drainage basins erode, from the Western Southern Alps of New Zealand, one of the fastest-eroding places on Earth. We find that the rate at which these drainage basins erode is best predicted by the proportion of their drainage area that falls within the 1,500–2,000 m above sea-level elevation window. This elevation range had previously been suggested to be where rocks are damaged and eroded through freeze-thaw cycles. It is also the elevation window from which glaciers are currently retreating or have recently retreated, which can intensify erosion. Both freeze-thaw cycles and glacier retreat depend on elevation and are related to temperature; therefore, we infer that temperature-controlled erosional processes have likely dominated erosion for the last decades to hundreds of years.

1. Introduction

In Earth's most rapidly uplifting landscapes, coupled landsliding and river incision (Burbank et al., 1996; Hovius et al., 1997; Larsen & Montgomery, 2012), and glacial erosion (Egholm et al., 2009; Herman et al., 2015) are thought to limit mountain height, linking tectonics and climate via climate-mediated erosion. As rock uplift progresses, mountains grow taller, inducing orographic precipitation and glaciation, which in turn facilitate erosion (Brozović et al., 1997; Pedersen et al., 2010; Whipple, 2009; Whipple et al., 1999). In glaciated landscapes, mountain elevations are limited at and above the elevation where ice accumulates. This observation is thought to be associated with intense scour beneath the glaciers (i.e., "the glacial buzzsaw") (Egholm et al., 2009;

Pedersen et al., 2010). There is also growing evidence for temperature-controlled erosion operating at similar or slightly lower elevations: paraglacial erosion, related to deglaciation and conditioned by the previous glaciated stage (S. K. Allen et al., 2009, 2011; Hartmeyer et al., 2020a), as well as periglacial erosion (i.e., frost cracking), related to freeze-thaw cycles (Delunel et al., 2010; Egholm et al., 2015; Hales & Roering, 2005). However, it is unclear whether paraglacial and periglacial processes can: (a) impact tectonic-climate interactions by substantially modulating erosion rates and balancing rapid rock uplift; (b) influence mountain topography by localizing efficient erosion; and/or (c) be coupled to tectonics by being more prevalent where rock-uplift is greater. These uncertainties arise because studies examining the impact of paraglacial and periglacial erosion processes are, so far, restricted to decadal timescales (S. K. Allen et al., 2009, 2011; Hartmeyer et al., 2020a) or areas with relatively low (<2 mm/yr) and uniform rock-uplift rates (Delunel et al., 2010; Draebing et al., 2022; Hales & Roering, 2005, 2009; Marshall et al., 2021; Savi et al., 2015).

The Western Southern Alps of New Zealand/Aotearoa are ideal for investigating how different erosional processes counteract some of the highest rock-uplift rates on Earth, given their order-of-magnitude differences in erosion rates along and across the strike of the range (Hicks et al., 2011; Hovius et al., 1997; Larsen et al., 2014; Nibourel et al., 2015; Wang et al., 2020), coupled with strong spatial variations in climate and rock-uplift rates (Lorrey et al., 2022; Norris & Cooper, 2001; Sattler et al., 2016; Tait & Macara, 2014; Tait et al., 2012). Fast and variable erosion on the west side of the range has been attributed to landsliding driven by strong rainfall (Hovius et al., 1997), or paraglacial mass wasting (S. K. Allen et al., 2009, 2011; Jiao et al., 2018) and glacial scouring (Herman et al., 2015). However, erosion studies in the Western Southern Alps have been restricted to very few catchments (Herman et al., 2015; Jiao et al., 2018; Larsen et al., 2014, 2023; Nibourel et al., 2015; Wang et al., 2020), decadal timescales (S. K. Allen et al., 2009, 2011; Hicks et al., 2011; Hovius et al., 1997), or to regions below the tree line (Hovius et al., 1997; Wang et al., 2020). Moreover, temperature-controlled frost cracking, found to play an important role in erosion east of the main drainage divide (Hales & Roering, 2005), has not been closely examined in the Western Southern Alps.

Erosion rates on 10^2–10^4 yr timescales are often quantified using in situ produced cosmogenic radionuclides (CRN). These nuclides (e.g., ^{10}Be, ^{26}Al, and ^{14}C) accumulate in minerals due to exposure to cosmic rays (Bierman & Steig, 1996; Lal, 1991; Schaefer et al., 2022). CRN production rates are greatest at the surface, and their concentrations increase with exposure time such that they are inversely related to denudation rates (Bierman & Steig, 1996; Lal, 1991; Schaefer et al., 2022). Denudation rates calculated from CRN concentrations in river sands integrate different processes acting across the catchment. Here, we present 20 new, plus 7 published (Larsen et al., 2014), catchment-averaged denudation rates derived from concentrations of in situ-produced ^{10}Be in fluvial sands from the Western Southern Alps. By comparing these data to published data from climate records, exhumation rates inferred from low-temperature thermochronology, sediment provenance, fault-slip rates, land-cover maps, and various topographic metrics, we examine the spatial distribution and controls of denudation, and we infer the dominant erosional processes at the orogen scale.

2. Climate-Mediated Erosional Processes: Main Controlling Variables and Limitations in Their Evaluation

In steady-state orogens, long-term (~10^6 yr) erosion rates balance rock-uplift rates, and hence are largely dictated by tectonics (Willett & Brandon, 2002). However, over timescales shorter than ~10^6 yr, climate cycles and their related erosional processes can influence rates and patterns of erosion (Delunel et al., 2010; Draebing et al., 2022; Herman et al., 2015; Marshall et al., 2015; Moon et al., 2011).

Precipitation has long been recognized as an important climate variable controlling erosion through its influence on river incision (Roe et al., 2003), surface runoff and associated sediment transport (Dadson et al., 2003), and landslide activity (Marc et al., 2018). The impact of precipitation is generally evaluated by comparing erosion or exhumation rates (over 10^0–10^6 yr timescales) or landslide rates (over 10^0–10^1 yr timescales) with measured precipitation rates or intensity (LaHusen et al., 2020; Moon et al., 2011; Schildgen et al., 2022). These data are often derived from a small number of weather stations that have recorded data over <10^2 yr, a timescale that is commonly shorter than the integration timescale of erosion-rate estimates.

Glaciers constitute another important climate-mediated erosional agent. Glacial erosion rates are mainly controlled by the shear rate at the ice-rock interface; however, given the challenges of measuring this variable,

many studies parametrize glacier erosion rates as a function of the ice sliding velocity and bedrock erodibility (Cook et al., 2020; Herman et al., 2015; Koppes et al., 2015). Ice sliding velocities depend on topography and the glacier's basal thermal regime (Kamb, 1970), which is influenced by mean annual temperature (Koppes et al., 2015) and precipitation (Cook et al., 2020). However, for a single ice sliding velocity value, glacial erosion rates can span several orders of magnitude (Cook et al., 2020; Koppes et al., 2015). Glacial erosion rates are typically estimated from sediment yields in streams or from proglacial sediment accumulations. Consequently, estimates are limited to $\leq 10^1$ yr timespans or to longer but poorly constrained time periods. This leads to uncertainties in the range of 10%–50% (Cook et al., 2020; Herman et al., 2015; Koppes et al., 2015) and lack of clarity on how to extrapolate the estimates to longer timescales that include changes in temperature and precipitation.

As glaciers shrink, the relative contribution of glacial erosion to total catchment erosion likely diminishes, while the relative importance of paraglacial erosion increases (Williams & Koppes, 2019). Paraglacial erosion is ultimately controlled by bedrock strength and air temperature, the latter of which influences rock temperatures, meltwater changes, and glacier retreat rates (Grämiger et al., 2017, 2020; Hugentobler et al., 2022). Landslides can contribute to paraglacial bedrock erosion, because as glaciers retreat and permafrost thaws, surrounding hillslopes experience changes in their thermal, hydraulic and mechanical boundary conditions that induce bedrock-stress changes (Hartmeyer et al., 2020a; Hugentobler et al., 2022). Base-level changes in tributaries to glacial valleys also promote incision (Williams & Koppes, 2019). Modeling, monitoring, and aerial imagery-based studies show that these processes lead to increased landslide frequencies and magnitudes in recently deglaciated areas (S. K. Allen et al., 2011; Draebing et al., 2022; Gruber et al., 2004; Hartmeyer et al., 2020a, 2020b; Hugentobler et al., 2022; Noetzli et al., 2003; Ravanel & Deline, 2011). These studies typically compare temporal and spatial changes in short-term (10^0–10^1 yr) erosion rates or landslide activity to the distance from the retreating glacier front or to the time since deglaciation. The latter requires detailed deglaciation histories, which are only available at a few sites (S. K. Allen et al., 2011; Williams & Koppes, 2019).

Periglacial processes (predominantly frost-cracking) occur commonly in regions experiencing paraglacial landscape adjustment, and they can help pre-condition bedrock for paraglacial landsliding (Draebing et al., 2022; Geng et al., 2022; Grämiger et al., 2017; Hartmeyer et al., 2020a). Compared to paraglacial landsliding, which represents lower-frequency, higher-magnitude erosional events that deliver a wide range of grain sizes, including meter-scale boulders (Ben-Yehoshua et al., 2022), periglacial frost-cracking represents higher-frequency, lower-magnitude erosional events that deliver narrower and finer grain size distributions (P. A. Allen et al., 2015; Sklar et al., 2017). Frost-cracking primarily occurs through segregation ice growth, whereby liquid water is attracted to ice lenses growing in bedrock fractures, increasing pore pressure (R. S. Anderson et al., 2013; Hales & Roering, 2007; Rempel et al., 2016). The rate of frost cracking by ice segregation is proportional to temperature gradients within the rock and the supply rate of liquid water (R. S. Anderson et al., 2013; Hales & Roering, 2007). Frost cracking is most efficient at rock temperatures within the "frost-cracking window" of −3°C to −8°C (R. S. Anderson, 1998; Walder & Hallet, 1985), but it can occur over a wide range of mean annual air temperatures (MAAT), provided that temperatures drop below 0°C frequently. Daily temperature fluctuations are attenuated by an order of magnitude within ∼35 cm of the surface, whereas seasonal fluctuations can affect the top few meters of bedrock (R. S. Anderson et al., 2013; Hales & Roering, 2007; Rempel et al., 2016). Snow or regolith cover reduces temperature fluctuations in the underlying bedrock. These insulating effects are limited on steep hillslopes where cover preservation is low (Andersen et al., 2015; R. S. Anderson et al., 2013). Bedrock strength, porosity and pre-existing fracture networks further modulate frost-cracking intensity (Andersen et al., 2015; Draebing & Mayer, 2021). Direct rock temperature measurements are only available in a few monitored sites (Draebing & Mayer, 2021; Draebing et al., 2022; Hartmeyer et al., 2020a), and variables such as snow/regolith cover, daily temperature cycles, bedrock strength, and fracture networks are challenging or impossible to constrain at the landscape scale and over >10^2 yr timescales. Consequently, studies comparing long-term (>10^2 yr) erosion rates to frost-cracking predictions generally use models that consider only MAAT and annual temperature fluctuations (Delunel et al., 2010; Geng et al., 2022; Hales & Roering, 2005, 2009; Marshall et al., 2015, 2021; Savi et al., 2015).

3. Study Area

3.1. Tectonics and Geology

The Southern Alps arise from oblique convergence between the Pacific and Australian plates (Figures 1a and 1b). Most convergence is accommodated as strike-slip motion on the range-bounding Alpine Fault, while
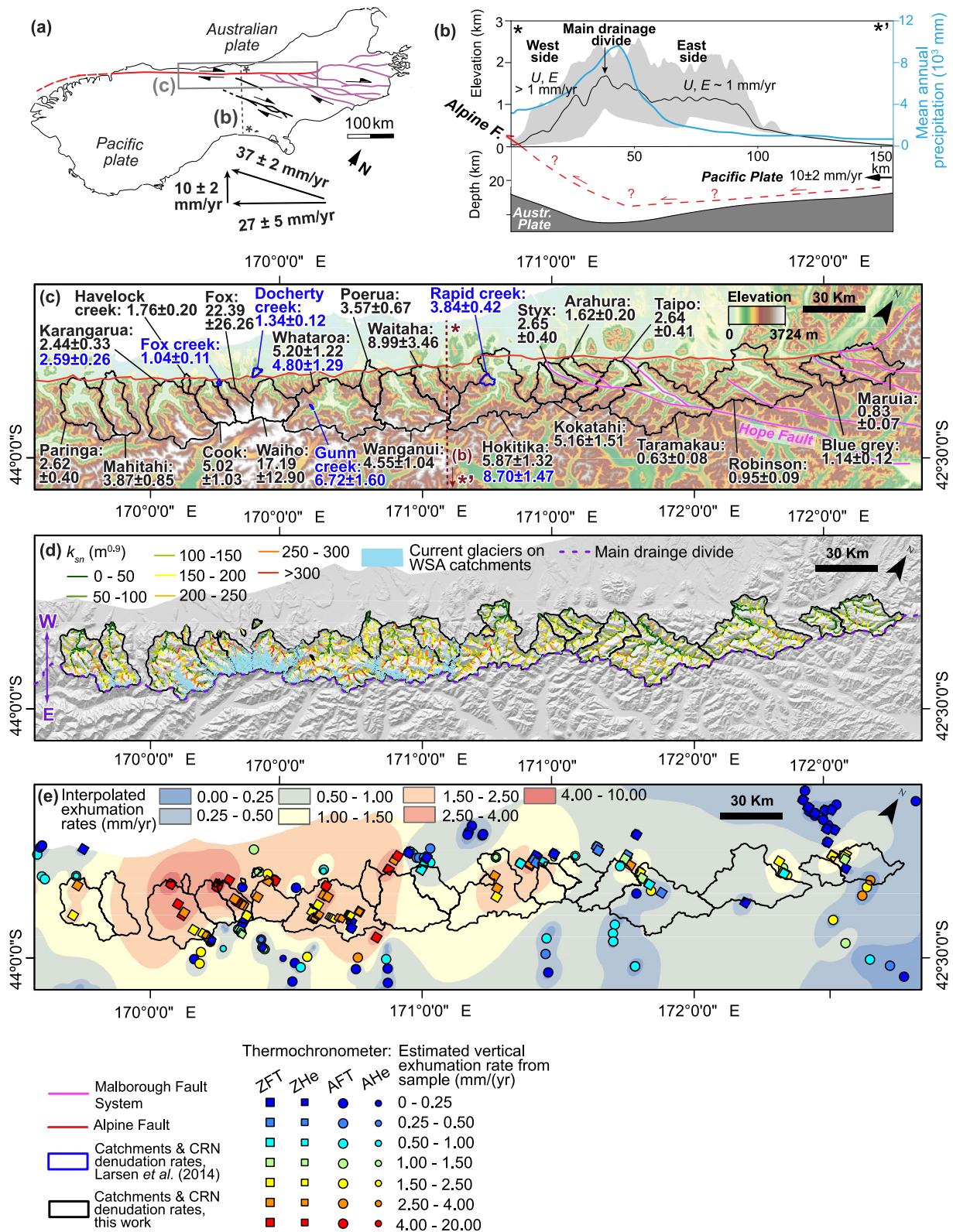
Figure 1.

10 ± 2 mm/yr of fault-normal motion induces rapid rock uplift in the Southern Alps, focused to the west of the range divide (Norris & Cooper, 2001) (Figures 1a and 1b). Along the strike of the Western Southern Alps, exhumation rates are highest in the central sector and decrease to the NE and SW, as well as to the east side of the range (Batt et al., 2000; Herman et al., 2009; Little et al., 2005) (Figure 1e). Although uncertainties in exhumation pathways (due to poor constraints on the Alpine Fault ramp geometry, Figure 1b) complicate converting cooling ages to exhumation rates, published work suggests rates of at least a few mm/yr for most Western Southern Alp catchments and at least ∼6–9 mm/yr within the central Waiho and Fox catchments, where relief is highest (Little et al., 2005). Late Quaternary throw rates (vertical component of fault slip rates) along the Alpine Fault are also highest in the central sector, up to 12 mm/yr, and decrease toward the SW and NE (Langridge et al., 2010, 2017; Norris & Cooper, 2001) (Figure 2a; Table S1 in Supporting Information S1). Perpendicular to this pattern, one NW-SE oriented transect across the Southern Alps shows that present-day inter-seismic elastic vertical deformation inferred from GPS observations is highest (∼5 mm/yr) at the main drainage divide, ∼20 km SE of the Alpine Fault (Beavan et al., 2010). Another study based on the displacement of mid-Holocene to last interglacial marine deposits suggests instead that rock uplift is fastest halfway across the range, ∼5–8 km SE of the Alpine Fault (Adams, 1980). The youngest thermochronometric cooling ages also tend to occur ≤10 km SE of the Alpine Fault (Batt et al., 2000; Herman et al., 2009; Little et al., 2005; Tippett & Kamp, 1993a, 1993b) (Figure 1e). In summary, there is a good agreement that along the Western Southern Alps (SW to NE), the fastest rock-uplift rates are located where relief is highest in the central sector of the range, and rates decay along strike to the SW and NE; whereas the distribution of rock uplift and absolute rock-uplift rates across the range (NW to SE) are debated.

The rocks in the hanging wall of the Alpine Fault in the Western Southern Alps are part of the Torlesse Composite Terrane, composed of Carboniferous to Cretaceous metamorphosed quartzofeldspathic graywackes (Beyssac et al., 2016; Heron, 2014). Owing to the different crustal levels from which rocks have been exhumed, the highest metamorphic grade rocks are exposed immediately east of the Alpine Fault, and progressively lower grades are found toward the main drainage divide and in the eastern Southern Alps (Beyssac et al., 2016; Heron, 2014) (Figure S1 in Supporting Information S1). This gradient in metamorphic grade enables sediment provenance analyses based on estimating peak metamorphic temperatures using Raman spectroscopy of carbonaceous material (Beyssac et al., 2016; Herman et al., 2015; Jiao et al., 2018; Nibourel et al., 2015). Because all lithologic units across the range have a similar quartzofeldspathic greywacke parent rock, we do not expect significant differences in their quartz content that could bias our CRN catchment-averaged denudation rates.

Fracture densities vary across the SA. Because of deeper exhumation and transpression along the Alpine Fault ramp (Figures 1a and 1b), bedrock in the Western Southern Alps is pervasively fractured, whereas bedrock on the eastern side of the range has a lower fracture density associated with shallower burial and exhumation trajectories (Clarke & Burbank, 2010).

3.2. Climate

The only available and widely used climate data from the SA are derived from seven weather stations that have been recording data for 20–99 years (Hales & Roering, 2005, 2007, 2009; Sattler et al., 2016). These stations show that median annual temperatures in the study area range between −3 and 16°C, median annual rainfall rates range between 2,300 and 13,000 mm, and median daily rainfall intensity ranges between 15 and 38 mm/day (Figures S2a–S2c in Supporting Information S1). Temperature varies with elevation (Figures S2d and S2e in Supporting Information S1), whereas precipitation rates are an order of magnitude higher in the Western Southern Alps than on the eastern side of the range (Figure 1b and Figure S2b in Supporting Information S1). The highest elevation station, at the Craigieburn Range Ski Field (1,554 masl), registers a MAAT of 3.7°C (Hales & Roering, 2007, 2009). Based on a lapse rate of 0.6 ± 0.1°C/100 m (Hales & Roering, 2005, 2007, 2009; Kaplan et al., 2013; Putnam et al., 2012), MAATs of ∼0–1°C would occur at 2,000 m above sea level (masl) in the study

Figure 1. (a) Location and tectonic context of the study area and (b) Elevation swath of the Southern Alps perpendicular to the range and Alpine Fault, both adapted from Little et al. (2005). (c) Western Southern Alps (WSA) catchments along the Alpine Fault with denudation rates (±1σ). New denudation rates from this work are in black, and those recalculated from Larsen et al. (2014) are in blue. The vertical dashed line with asterisks marks the location of the cross section in (b). (d) Normalized channel steepness index values (k_{sn}) for 1-km-long segments and current glacier extents for the studied catchments. The purple-dashed line marks the position of the main drainage divide that separates the western wet side from the eastern, drier side of the range (b). (e) First-order exhumation rate estimates for cooling ages of the zircon fission-track, ZHe, apatite fission-track, and AHe systems, plotted on top of a map interpolating exhumation rates based on all sample values.
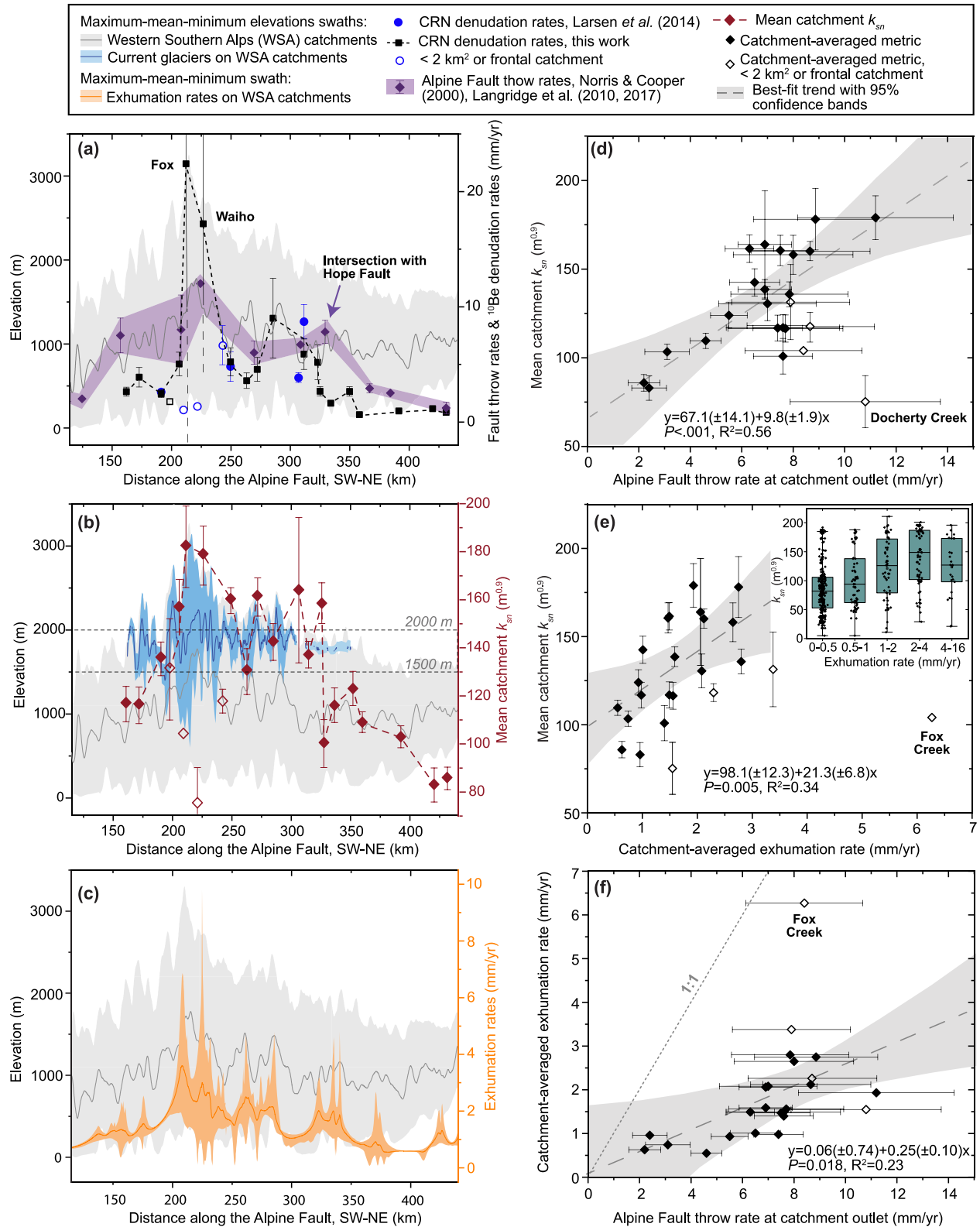
Figure 2.

area. Annual temperature fluctuations are consistently ∼12°C at all weather stations; hence, the annual temperature amplitude is ∼±6°C (Hales & Roering, 2007).

Although the timing and magnitude of the Little Ice Age (LIA) cooling in the SA is debated, its peak impact is thought to have occurred at ∼1600–1725 CE, with a minimum cooling of −1 to −1.2°C and a lowering of snowlines by ∼160–200 m elevation (Lorrey et al., 2022; McKinzey et al., 2004; Winkler, 2000) compared with present day conditions. At the end of the LIA, and possibly for a few decades afterwards, snowlines were likely ∼100 m lower than today (Figure 1d and Figure S3a in Supporting Information S1), implying that since then, MAAT has increased by ∼0.6°C and isotherms have shifted vertically by +100 m (Kaplan et al., 2013; Putnam et al., 2012). Net snowline recession is estimated to be ∼140 vertical m in the last 500 yr (Putnam et al., 2012), ∼420–340 vertical m in 14.5 ka (Kaplan et al., 2013), and ∼880 vertical m since the Last Glacial Maximum (LGM) at 19.8 ka (Tielidze et al., 2022). Climate models based on observed glacial extents suggest that precipitation has probably not changed significantly during the late Holocene (B. Anderson & Mackintosh, 2006; Kaplan et al., 2013).

3.3. Erosion Rates, Patterns, and Processes

Several methods have been used to estimate erosion rates in the Western Southern Alps. Catchment-averaged erosion rates inferred from suspended sediment yields, based on measurements between the 1960s and 1990s (Hicks et al., 2011) are 0.2–6.7 mm/yr (Table S3 in Supporting Information S1). The few previously published CRN catchment denudation rates, representative of denudation over the last ∼240 yr on average, mostly fall within this range (Larsen et al., 2014, 2023) (Figure 1c; Table S3 in Supporting Information S1). Of these measurements, three were made in major catchments (Karangarua, Whataroa, and Hokitika), and five in small tributaries, of which two are <2 km^2 and one is <0.5 km^2. CRN-derived soil erosion rates from 13 soil pits in mountain ridges range between ∼0.1 and 1 mm/yr, except for one sample suggesting erosion at 2.5 mm/yr (Larsen et al., 2014, 2023). In these studies, soil erosion and production were found to be dominantly controlled by catchment denudation rates, which control sediment residence times (Larsen et al., 2014, 2023). Lake sedimentation rates (Howarth et al., 2014) and coseismic landslide modeling (Robinson et al., 2016) suggest that long-term erosion rates over a full seismic cycle could be ∼40%–50% higher than inter-seismic estimates.

The distribution of erosion across the strike in the Western Southern Alps (NW-SE) is thought to be non-uniform, but available measurements are insufficient to determine whether erosion rates are highest close to the fault or at specific elevations (Jiao et al., 2018; Nibourel et al., 2015; Wang et al., 2020), either of which could have implications for the processes contributing to erosion. The two available Raman spectroscopy-based sediment-provenance studies suggest different erosion patterns. One study from the Whataroa catchment (Figure 1c) suggests maximum erosional intensity ∼10 km SE of the Alpine Fault, possibly due to localization of inter-seismic strain or orographic precipitation (Nibourel et al., 2015). The other study, involving analysis of an offshore sediment core, suggests that enhanced erosion occurs in the upper, recently deglaciated valleys due to paraglacial hillslope response (Jiao et al., 2018).

The Western Southern Alps were fully glaciated during the LGM, and glacial erosion is still important in the Fox and Waiho catchments (Herman et al., 2015). Fox glacier currently extends down to 420 masl and Franz Josef

Figure 2. Profiles of the Western Southern Alps along the strike of the Alpine Fault; with (a) elevation swath, denudation rates (±1σ) and fault throw rates (error bars represent uncertainties reported in the source publications). Throw rates are from Norris and Cooper (2001) and Langridge et al. (2010, 2017). For details on the methods, source data, uncertainties and assumptions, see the source papers indicated for each locality in Table S1 in Supporting Information S1, which provides a summary of these data. X = 0 km is the point where the Alpine Fault intersects the coastline near Mildford Sound. A portion of the ^{10}Be denudation rate uncertainty for Fox and Waiho is dashed (here and elsewhere) because it is unlikely that these catchments have denudation rates <9 mm/yr (see text). (b) Elevation swath, swath of glacial extent elevations, and mean catchment k_{sn}. (c) Elevation swath plotted again for reference, together with a swath of first-order exhumation rates along the range, produced from the interpolated exhumation map in Figure 1e. Mean catchment k_{sn} plotted against fault throw rates at catchment outlets (d) and catchment-averaged exhumation rates (e). Throw rates at the catchment outlets have been estimated based on the throw rate curve of (a) and the distance along the Alpine Fault of each catchment outlet (Table 1). The catchment outlet position was selected because tectonic signals are expected to propagate upstream from this point (e.g., Roda-Boluda et al., 2019). The uncertainty of each catchment outlet throw rate was estimated based on the average of the relative uncertainties of the nearest throw rate data points to the SE and NW (Table S1 in Supporting Information S1, Table 1). Some throw rate localities do not have an uncertainty estimate published (Table S1 in Supporting Information S1); in that case, the relative uncertainty of the following nearest locality was used. The clear outlier in each case (Docherty creek for (d) and Fox Creek for (e)) was excluded from the regression. The inset in (e) shows a box plot of k_{sn} values for binned exhumation rates, extracted for each thermochronological sample location from the interpolated k_{sn} map in Figure S4 in Supporting Information S1. For more information regarding the uncertainties in exhumation rates, see the methods section. (f) Catchment-averaged exhumation rates against throw rates at the catchment outlet.

Table 1
Tectonic, Topographic, and Climate Metrics of the Studied Catchments

Catchment	Area (km²)	Throw rate at catchment outlet (mm/yr)	Catchment-averaged exhumation rate, ZFT, ZHe, AFT, AHe combined (mm/yr)	Mean elevation (m)	Maximum elevation (m)	Relief (m)	Mean slope (°)	% Of slopes >32°	Mean ksn (m⁰·⁹)	% Of area in the 1,500–2,000 m elevation window
Paringa	232.1	7.6 ± 2.2	1.5	855	2,566	2,539	25.6	31.0	117 ± 7	9.6
Mahitahi	174.5	7.7 ± 2.2	1.6	917	2,638	2,623	25.6	31.6	116 ± 8	13.1
Karangarua	361.1	7.9 ± 2.3	2.8	1,159	3,081	3,053	27.3	35.8	136 ± 7	19.3
Havelock Creek	13.9	7.9 ± 2.3	3.4	773	1,832	1,782	25.2	30.3	131 ± 21	3.1
Cook	128.6	8.0 ± 2.3	2.7	1,296	3,463	3,346	28.0	40.2	158 ± 11	19.1
Fox Creek	1.6	8.4 ± 2.3	6.3	744	1,201	1,011	28.2	28.6	104 ± 0	0.0
Fox	91.8	8.9 ± 2.4	2.8	1,623	3,413	3,238	22.9	30.7	178 ± 17	25.6
Docherty Creek	6.4	10.8 ± 2.9	1.6	399	749	644	15.1	0.0	75 ± 15	0.0
Waiho	163.2	11.2 ± 3.0	1.9	1,513	3,074	2,923	24.7	30.0	179 ± 12	26.0
Gunn Creek	1.5	8.7 ± 2.3	2.3	899	1,524	1,200	29.7	34.1	118 ± 5	1.4
Whataroa	448.2	8.7 ± 2.3	2.1	1,213	3,068	2,974	26.0	28.8	160 ± 5	25.7
Poerua	83.9	7.0 ± 1.9	2.1	1,002	2,362	2,288	25.9	31.2	131 ± 10	15.4
Wanganui	341.2	6.3 ± 0.9	1.5	1,209	2,620	2,529	25.6	27.8	162 ± 8	25.2
Waitaha	154.7	6.5 ± 1.0	1.0	851	2,567	2,555	25.5	28.0	142 ± 8	25.0
Rapid Creek	12.8	6.9 ± 1.0	2.1	1,046	1,966	1,834	27.2	26.4	164 ± 30	9.2
Hokitika	433.7	6.9 ± 1.0	1.6	1,015	2,556	2,511	24.2	23.0	139 ± 6	18.3
Kokatahi	100.8	7.5 ± 1.1	1.5	1,048	2,027	1,957	26.0	25.3	161 ± 9	19.4
Styx	56.4	7.6 ± 1.1	1.4	805	1,883	1,798	24.7	25.1	101 ± 10	6.2
Arahura	126.0	7.4 ± 1.0	1.0	951	1,945	1,799	24.5	20.2	117 ± 7	9.1
Taipo	182.3	5.5 ± 0.7	0.9	986	2,144	2,016	24.4	21.7	124 ± 7	12.7
Taramakau	460.1	4.6 ± 0.6	0.6	972	2,232	2,064	24.7	25.4	110 ± 4	9.5
Robinson	453.7	3.1 ± 0.9	0.7	884	1,794	1,637	23.0	18.8	103 ± 4	3.1
Blue Grey	97.5	2.4 ± 0.7	1.0	1,051	1,761	1,342	22.4	16.7	83 ± 7	4.6
Maruia	218.9	2.2 ± 0.6	0.6	1,075	2,029	1,572	22.7	15.4	86 ± 5	8.6

Note. Catchments in italics are those sampled by Larsen et al. (2014). Residual values correspond to the *observed y* minus *predicted y* of the regression of ¹⁰Be denudation rates versus throw rates at catchment outlet in Figure 3a, and versus catchment-averaged exhumation rates in Figure 3b, respectively. Catchment with no residual value were excluded from the regressions.

% Of area glaciated	% Of area glaciated if glaciers are lowered 100 m (~275 years ago)	% Of catchment area with bare bedrock	Median annual air temperature, MAAT (°C)	Median annual rainfall (mm)	Median rainfall intensity (mm/day)	% Of area with a 0-4°C MAAT (PPEw)	Residual values from regression in Figure 3a (mm/yr)	Residual values from regression in Figure 3b (mm/yr)
4.1	5.9	34.0	7.4	7,889	37	12.1	−0.99	−0.73
5.1	8.1	38.4	7.1	8,130	37	15.6	0.23	0.48
12.4	15.8	48.1	6.1	8,608	35	26.2	−1.26	−1.86
0.0	0.0	19.7	7.5	5,614	30	7.3	−1.96	−2.96
19.2	23.0	46.3	5.4	9,545	35	28.9	1.27	0.83
0.0	0.0	0.0	7.8	5,154	28	0.0	–	–
49.7	53.1	34.7	3.9	9,429	35	57.9	–	–
0.0	0.0	0.0	9.8	4,959	28	0.0	−3.44	−2.05
41.6	42.3	34.7	4.4	10,337	36	54.8	–	–
0.0	0.0	18.0	8.2	7,093	31	0.0	–	–
13.4	17.4	48.0	6.1	8,077	30	34.7	1.21	1.40
2.3	3.0	41.4	6.5	5,922	27	20.4	0.19	−0.21
13.7	16.3	44.5	5.6	7,654	30	36.6	1.43	1.20
5.4	7.7	50.2	5.7	7,399	32	34.3	5.79	5.99
0.0	0.0	36.5	6.5	9,648	32	5.6	0.49	0.08
3.4	4.5	42.0	6.6	6,705	27	23.5	2.53	2.45
0.7	1.4	49.5	6.3	9,019	33	24.7	1.59	1.83
0.0	0.0	22.3	7.4	8,875	33	6.6	−0.95	−0.63
0.1	0.1	39.8	6.6	9,610	34	12.0	−1.91	−1.35
0.6	1.2	48.1	6.5	7,730	32	16.7	−0.19	−0.30
0.1	0.2	45.8	6.7	4,911	26	10.9	−1.87	−2.04
0.0	0.0	30.0	7.5	3,088	19	0.2	−0.99	−1.85
0.0	0.0	38.4	7.0	3,205	20	0.0	−0.54	−1.82
0.0	0.0	30.9	7.0	2,628	17	1.7	−0.78	−1.90

glacier (in the Waiho catchment) to 593 masl (Baumann et al., 2021) (Figures 1c and 1d; Table 1). Estimates of glacial erosion rates in the Waiho catchment based on ice-sliding velocities and suspended sediment load observations over several months show spatial variations between 0 and 25 mm/yr (Herman et al., 2015). Estimates of glacier erosion rates are unavailable for other catchments. Equilibrium Line Altitude (ELA) estimates in other Western Southern Alps "index glaciers," based on observations of end-of-summer snowline elevations between 1981 and 2010, are on average ~1,780 ± 100 masl (Lorrey et al., 2022). Current permafrost is estimated to extend down to ~2,000 masl on shaded hillslopes, and a few hundred meters higher on sunny hillslopes (S. K. Allen et al., 2009; Sattler et al., 2016), with degrading permafrost likely occurring 100–150 m below these limits (S. K. Allen et al., 2009). Compared to the wide glacial valleys on the east side of the range, there is relatively little moraine material preserved in the narrow, steep-sided valleys of the Western Southern Alps (Barrell, 2011).

Landslides have been highlighted as an important erosion process in the Western Southern Alps. Hovius et al. (1997) reported landslide erosion rates in the range of 1.8–18 mm/yr for the catchments between Paringa and Waitaha (Table S3 in Supporting Information S1). This landslide inventory is based on landslide mapping below the treeline between 1948 and 1986, but it is extrapolated to kiloyear timescales using a frequency-magnitude relationship. Based on an expansion of this landslide inventory to the period 1935–2014, Emberson et al. (2016) calculated landslide volumes for the catchments between Paringa and Waitaha using a more refined regional landslide area-volume scaling relationship estimated by Larsen et al. (2010). Landslide erosion rates averaged across the 79-yr observation period amount to 0.15–1.25 mm/yr (Table S3 in Supporting Information S1). Landsliding is reportedly most frequent just below permafrost elevations, attributed to permafrost degradation and hillslope adjustment following glacial retreat (S. K. Allen et al., 2009, 2011; Jiao et al., 2018). However, only one landslide inventory of limited size ($n = 509$) and short duration extends above the treeline (~1,400 m) (S. K. Allen et al., 2011), precluding robust conclusions about erosion patterns just below the permafrost zone (~2,000 m).

Active scree, potentially produced by frost-cracking (Hales & Roering, 2005, 2007, 2009), covers <10% of the Western Southern Alps hillslopes, increasing up to 20% on the highest ridges. Vegetated scree is rare in the Western Southern Alps (Hales & Roering, 2005, 2009). On the eastern side of the range, where frost-cracking has been suggested to be the dominant erosional mechanism, 20%–30% of hillslopes are covered by active scree, and up to 70% by vegetated scree (Hales & Roering, 2005, 2009). It is unclear if these differences across the range arise from the Western Southern Alps having less terrain at elevations susceptible to frost-cracking or higher precipitation rates (Figure 1b) that drive a more efficient removal of scree (Hales & Roering, 2009). Denudation rates on frost-cracking-dominated hillslopes of the eastern Southern Alps have been estimated to reach up to 0.30–0.86 mm/yr (Hales & Roering, 2009). Based on a segregation ice model that considers MAAT and the amplitude of annual temperature fluctuations, maximum depth-integrated frost-cracking intensity in the Southern Alps is predicted between ~1,550 and 2,000 masl (Hales & Roering, 2007, 2009). This modeled frost-cracking window is supported by mapping of frost-cracking-derived scree, which is consistently found at elevations of 1,450 ± 250 masl, just beneath the modeled frost-cracking window (Hales & Roering, 2005, 2009). Given that this published model seems to capture the frost-cracking dynamics of the study area well (Hales & Roering, 2005, 2009), and in the absence of multi-year rock temperature, snow, or regolith cover constraints for the study area that would enable updating the model, we assume that frost cracking throughout the Southern Alps is concentrated between ~1,550 and 2,000 masl.

4. Methods

4.1. ¹⁰Be Sample Collection, Preparation, and Measurement

We collected river sand samples in November 2017 from exposed fluvial bars ~300 m around the sampling points listed in Table 2. Locations were chosen to be as close as possible downstream from the Alpine Fault, but not immediately downstream from recent landslides. The 125–710 μm grain size fraction was processed in the GeoForschungsZentrum (GFZ) Potsdam HELGES laboratory following standard cosmogenic nuclide sample preparation procedures (Nishiizumi et al., 1989; Von Blanckenburg et al., 2004; Wittmann et al., 2016). Analytical procedures and treatment of AMS data and uncertainties are detailed in Supporting Information S1, and the outlines of the catchments and raw CRN data are available in the Zenodo online repository (https://zenodo.org/record/8385574) and the Octopus CRN data base (https://octopusdata.org/).

Catchment-averaged denudation rates were calculated using the Basinga ArcGIS toolbox (Charreau et al., 2019), assuming a rock density of 2.7 g cm⁻³. A SLHL (Seal Level High Latitude) reference production rate of

Table 2
Information of the New Cosmogenic Radionuclide Samples Processed for This Manuscript and Calculated Catchment-Averaged Denudation Rates

Catchment	Latitude (°S)	Longitude (°E)	Measured ^{10}Be/^{9}Be ± $1\sigma^a$	Quartz dissolved (g)	^{9}Be carrier mass added $(10^{-4}$ g)	^{10}Be concentration ± 1σ (at/g)[b]	Catchment-averaged spallogenic production rate (at/g/yr)	Catchment-averaged muogenic production rate (at/g/yr)	Catchment-averaged denudation rate ± 1σ (mm/yr)	Integration time (yr)
Paringa	43.7088	169.4899	2.80E−14 ± 2.41E−15	111.050	1.372	2,035 ± 281	7.771	0.053	2.62 ± 0.40	229
Mahitahi	43.6394	169.5854	1.99E−14 ± 2.50E−15	105.283	1.362	1,426 ± 300	8.075	0.054	3.87 ± 0.85	155
Karangarua	43.5737	169.8020	2.97E−14 ± 2.14E−15	102.614	1.377	2,361 ± 289	8.542	0.052	2.44 ± 0.33	246
Havelock Creek	43.5207	169.8624	3.93E−14 ± 2.56E−15	110.063	1.375	3,002 ± 296	7.658	0.055	1.76 ± 0.20	341
Cook	43.4984	169.9661	1.86E−14 ± 1.78E−15	122.736	1.364	1,132 ± 221	8.516	0.049	5.02 ± 1.03	112
Fox	43.4793	170.0128	5.62E−15 ± 1.12E−15	125.193	1.364	163 ± 191	5.481	0.031	22.39 ± 26.26	25
Waiho	43.3923	170.1794	3.16E−15 ± 8.50E−16	125.980	1.386	−12 ± 183[c]	6.299	0.036	17.19 ± 12.9	33
Whataroa	43.2932	170.4133	1.68E−14 ± 1.92E−15	106.697	1.383	1,169 ± 263	9.024	0.053	5.20 ± 1.22	115
Poerua	43.1746	170.5048	2.42E−14 ± 2.78E−15	110.376	1.362	1,712 ± 303	9.005	0.057	3.57 ± 0.67	168
Wanganui	43.1631	170.6276	1.63E−14 ± 1.55E−15	92.850	1.371	1,279 ± 280	8.614	0.052	4.55 ± 1.04	132
Waitaha	43.0968	170.7281	1.07E−14 ± 1.38E−15	109.393	1.368	611 ± 229	7.958	0.054	8.99 ± 3.46	67
Hokitika	42.9158	170.9823	1.64E−14 ± 1.49E−15	113.835	1.372	1,047 ± 226	9.034	0.057	5.87 ± 1.32	102
Kokatahi	42.8946	171.1344	1.81E−14 ± 3.47E−15	107.621	1.369	1,254 ± 358	9.541	0.059	5.16 ± 1.51	116
Styx	42.8837	171.1542	2.65E−14 ± 2.05E−15	104.902	1.367	2,017 ± 275	7.759	0.055	2.65 ± 0.40	226
Arahura	42.8269	171.2336	4.35E−14 ± 3.65E−15	100.772	1.371	3,652 ± 394	8.701	0.057	1.62 ± 0.20	370
Taipo	42.7546	171.4024	3.06E−14 ± 2.99E−15	107.294	1.369	2,319 ± 328	9.007	0.058	2.64 ± 0.41	227
Taramakau	42.7401	171.5118	7.45E−14 ± 8.02E−15	67.695	1.369	9,611 ± 1,143	8.866	0.058	0.63 ± 0.08	958
Robinson	42.5347	171.8109	6.30E−14 ± 3.84E−15	92.981	1.373	5,887 ± 458	8.166	0.056	0.95 ± 0.09	632
Blue Grey	42.4104	172.1186	6.41E−14 ± 4.49E−15	101.579	1.370	5,473 ± 468	9.188	0.059	1.14 ± 0.12	528
Maruia	42.3436	172.2232	9.23E−14 ± 4.51E−15	105.447	1.359	7,659 ± 460	9.371	0.059	0.83 ± 0.07	725

^{a}Standards used (nominal ^{10}Be/^{9}Be values): KN01-6-2 (5.35 × 10^{-13}), KN01-5-3 (6.320 × 10^{-12}). ^{b}Corrected for a long-term average blank ^{10}Be/^{9}Be value of 4.52 × 10^{-15} ± 9.27 × 10^{-16} (3.08 × 10^4 ^{10}Be atoms) based on 15 processed blanks on Western Southern Alps sample batches. ^{c}Atom counts for this sample were below the blank counts. To estimate the erosion rate, we used a maximum blank-based ^{10}Be concentration of 244 at/g.
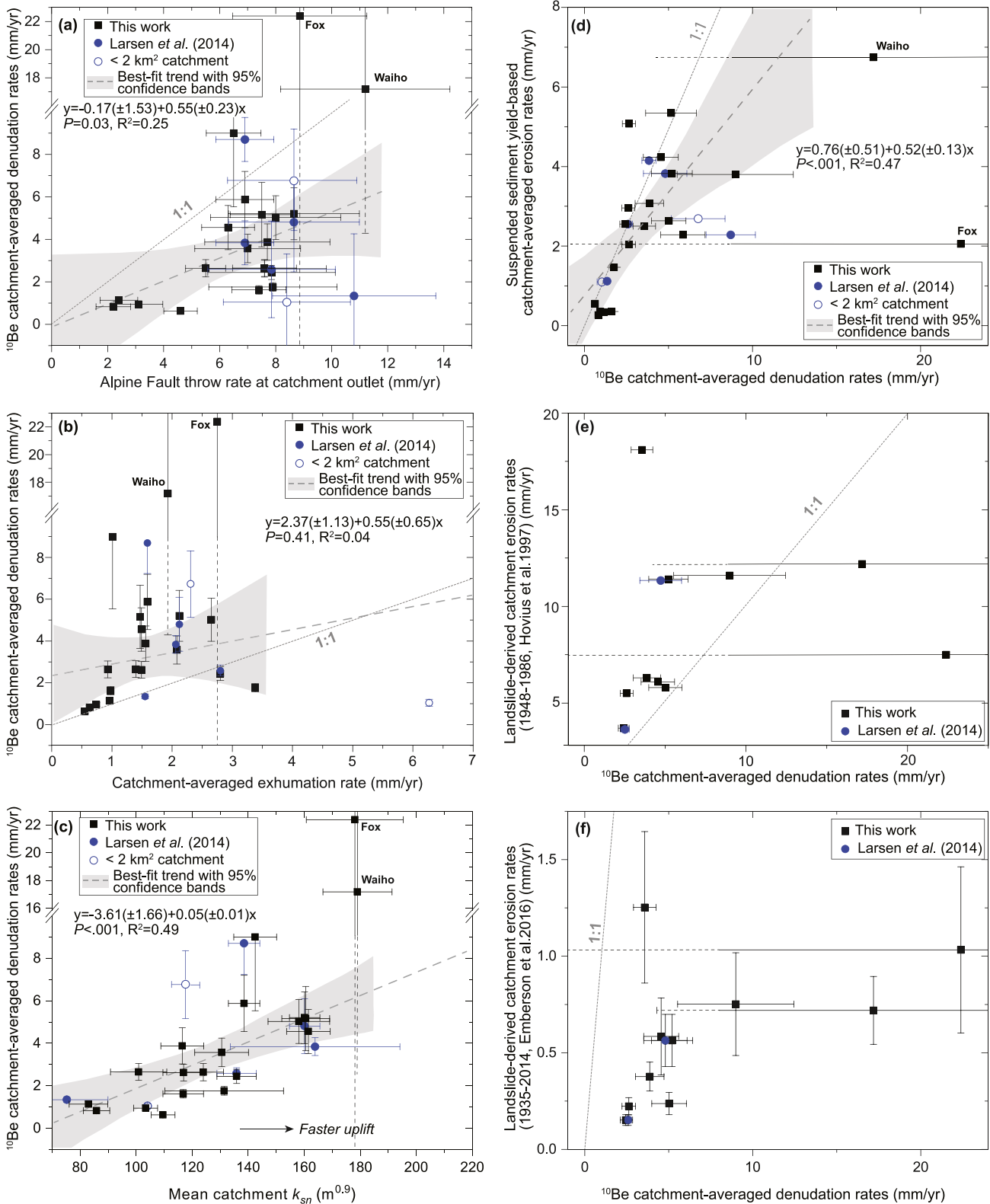
Figure 3.

3.84 ± 0.08 at g^{-1} yr^{-1} has been calibrated locally in the Southern Alps by Putnam et al. (2010) using the Lal/Stone scaling model. This value was used to calculate catchment-averaged ^{10}Be production from the production rates of each pixel in the catchment (Table 2). Catchment production rates were calculated assuming that current glacier cover (Figure 1d) completely shields the bedrock surface from cosmic rays. No topographic shielding correction was applied following recommendations from DiBiase (2018). Likewise, no snow cover corrections were applied, given that data on snow pack thickness in the steep terrain of the Western Southern Alps are not available. Nevertheless, in studies from other locations where snow cover data were available, snow was estimated to reduce the CRN production by <15% (Gosse et al., 1995; Schildgen et al., 2005; Wittmann et al., 2007). This value is lower or similar to common denudation rate uncertainties in fast-eroding settings. The integration timescale over which our catchment-averaged denudation rates are representative was calculated based on the time required to erode one e-folding length, $z^* = \Lambda/\rho \approx 60$ cm of the ^{10}Be production profile, where Λ is the attenuation length of 160 g cm^{-2} for spallation production, and $\rho = 2.7$ g cm^{-3} is the bedrock density (Lal, 1991; von Blanckenburg, 2005).

Published catchment-averaged ^{10}Be denudation rates from Larsen et al. (2014, 2023) were recalculated using the same density, reference production rate, scaling scheme, and ice mask (Table S3 in Supporting Information S1). We excluded from our analyses the Gunn Ridge north-draining tributary (Larsen et al., 2023), because its drainage area of 0.5 km^2 is four orders of magnitude lower than most of our sampled catchments. We include the other two bigger tributaries (Table 1), in our plots for reference, but exclude them from our analyses because (a) These creeks are smaller than our observed ~2 km^2 drainage area threshold for fluvial channel initiation, thus they do not meet our criteria for calculating channel steepness index (see Section 4.3 below); (b) In landslide-prone settings, ^{10}Be denudation rates from such small catchments are unlikely to be representative of long-term denudation rates (Niemi et al., 2005; Yanites et al., 2009). However, we incorporate Larsen's et al. (2014, 2023) complementary data set from soils and small tributaries into our discussion later.

4.2. Exhumation Rates

To estimate exhumation rates over the last few Myr, we compiled and reinterpreted 490 published zircon fission-track (ZFT), zircon (U-Th)/He (ZHe), apatite fission-track (AFT), and apatite (U-Th)/He (AHe) cooling ages (Table S2 in Supporting Information S1). Reported AFT cooling ages of 0 Myr were excluded; these ages are indicative of fast exhumation but do not provide quantitative constraints on exhumation rates. Cooling ages were converted to steady-state, vertical exhumation rates using the *age2exhume* script (van der Beek & Schildgen, 2023), with an initial geotherm of 25°C/km, a thermal diffusivity of 30 km^2/Myr, a model thickness of 25 km, a temperature at 0 masl elevation of 14°C and a lapse rate of 5°C/km. To correct for local topographic relief and surface-temperature variations, we follow Willett and Brandon (2013) in considering each sample's position relative to a smoothed version of the topography, with a smoothing radius defined by $\pi \times z_c$, with z_c being an estimated closure depth. The estimated z_c for each system was as follows: 2,000 m (AHe), 3,500 m (AFT), 5,000 m (ZHe), and 6,000 m (ZFT). Details on the model and parameters of each thermochronological system can be found in van der Beek & Schildgen (2023). Because the model assumes steady rock uplift and constant topography, it provides only first-order estimates of exhumation rates and regional patterns of exhumation.

We produced an interpolated map of exhumation rates as a reference for long-term rock-uplift rates, combining samples from the ZFT, ZHe, AFT, and AHe systems to maximize spatial coverage. This interpolation was done using the IDW tool in ESRI's ArcMap with the inverse distance weighted technique, using a minimum of four data points within a maximum search radius of 20 km. Catchment-averaged exhumation rates were estimated from the interpolated map. Interpolated maps using only ZFT or AFT data (the only two thermochronometric systems with sufficient spatial coverage) produce very similar patterns and rates (Figure S4, Table S3 in Supporting Information S1). Cooling ages have an associated uncertainty that results in a range of possible exhumation-rate

Figure 3. ^{10}Be catchment-averaged denudation rates compared to: (a) throw rates at the catchment outlet; (b) catchment-averaged throw rates; (c) mean catchment k_{sn}, a proxy for uplift rates; (d) suspended sediment yield-based catchment-averaged erosion rates (Table S3 in Supporting Information S1). These are derived from a raster that interpolates river suspended sediment yield data, produced by New Zealand's National Institute of Water and Atmospheric Research (NIWA). The raster is based on sediment-yield data from 233 New Zealand catchments collected between the 1960s and 1990s; for raw data and details on the model construction, see Hicks et al. (2011). To convert sediment yields (t km^{-2} yr^{-1}) into erosion-rate estimates (mm yr^{-1}), we assumed a rock density of 2.7 g cm^{-3}. (e) Long-term estimates of landslide erosion rates from Hovius et al. (1997); (f) decadal estimates of landslide erosion rates based on landslide volumes and associated uncertainties from Emberson et al. (2016). 1:1 lines shown for reference. In each panel, the metric integrating over a longer period of time is plotted on the *x*-axis, and the one integrating over a shorter timescale on the *y*-axis.

estimates (Table S2 in Supporting Information S1); for our analyses, we use the intermediate exhumation-rate estimate. Systematic uncertainties in exhumation rates relate to the unknown geometry of the Alpine Fault ramp, but those are difficult to quantify.

4.3. Topographic Analyses

To complement the exhumation-rate estimates, we measured geomorphic variables that can also reflect differences in rock-uplift rates (Table 1). We used the 90-m resolution SRTM DEM (Van Zyl, 2001) because the 30-m resolution SRTM and ASTER DEMs have either numerous holes or elevations that do not match the known elevations of several peaks in the Southern Alps.

For each of the CRN sample collection points, we extracted the DEM of the upstream catchment (Figure 1c, Table 2). For each catchment, we calculated the elevation distribution, catchment area, topographic relief and slopes in ESRI's ArcMap 10.7 using the Spatial Analyst toolbox. Using the slope map, we calculated the proportion of catchment areas steeper than the threshold hillslope angle of 32° for the Western Southern Alps (Clarke & Burbank, 2010). We observe that fluvial processes become dominant in drainage areas >2 km^2; for all catchments larger than this threshold, normalized channel steepness indices, k_{sn}, were calculated with the Topographic Analysis Kit, TAK (Forte & Whipple, 2019) for TopoToolbox (Schwanghart & Scherler, 2014), using a channel segment length of 1 km and a reference concavity value $\theta = 0.45$ ($k_{sn} = A^\theta S$, where A is drainage area and S is channel slope). The average concavity of the rivers in our study area was $\theta = 0.52$; however, we opted for using the more widely used value of 0.45 because this value does not alter the main patterns of k_{sn}, and it facilitates comparison with other studies. Glaciated parts of the catchment were excluded from catchment mean k_{sn} calculations. Uncertainties in the mean catchment k_{sn} values correspond to the standard errors of the mean k_{sn}. We also produced a map with interpolated k_{sn} values with TAK, by spatially averaging k_{sn} values within a 5-km circular moving window, to explore the relationship between exhumation rates at their sampling points and k_{sn} (Figure S4a in Supporting Information S1).

4.4. Data Plotting, Analyses, and Regressions

Plots, regressions, and calculations of the coefficient of determination (R^2) and P-values shown on the plots were performed using OriginPro 2018. We opted for not using weighted regressions because CRN denudation-rate uncertainties (both absolute and relative) are systematically correlated with the magnitude of the estimated denudation rate. We found that error-weighted regressions were not a good representation of our entire data set because they placed disproportionate importance on the lowest denudation rates with low uncertainties and practically ignored data points with denudation rates >3 mm/yr. For catchments with repeated measurements (Karangarua, Whataroa, and Hokitika; sampled both in this paper and in Larsen et al., 2014), we proceeded to the analyses using our ^{10}Be denudation rate value because it was obtained during the same sampling campaign as the rest of our data set.

To explore possible patterns of non-uniform erosion across the range (i.e., perpendicular to the strike of the Alpine Fault), we searched for the distance-from-fault surface trace or elevation windows that best correlate with our ^{10}Be denudation rate data set for different combinations of central values and window sizes. This was done in MATLAB using the binned distribution of elevations or distance-from-fault values of each catchment (using bin sizes of 100 and 500 m, respectively). To search for the distance-from-fault window that best correlates with ^{10}Be denudation rates, a raster with the minimum distance from the fault for each pixel was generated with ArcGIS, and the distribution of distance-from-fault values was extracted for each catchment. To search for the optimized elevation windows, we considered the hypsometry of each catchment. The output of the MATLAB script (which can be found as a file in Supporting Information S1 and in the Zenodo online repository: https://zenodo.org/record/8385574) is a matrix that shows the goodness-of-fit (R^2) that results from comparing ^{10}Be denudation rates with different elevations and distance-from-fault windows.

We tested for combinations of some independent variables that could predict denudation rate variability better than a single variable via stepwise regression. For details and results on this method, see the Supporting Information S1.

5. Results

Our sampled catchments cover a wide range of exhumation rates, uplift rates, and climate conditions, such that the influence of these parameters on denudation rates can be evaluated via regression analyses (Table 1). In

this section, we start by presenting and comparing published and new constraints on rock-uplift rates along the Western Southern Alps. To identify the relative importance of different erosional processes and their potential climatic and tectonic controls, we compare our new CRN denudation rates to these rock-uplift rate proxies, published erosion rates, published climate data, and our topographic metrics. We then examine whether erosion may be enhanced at certain distances from the Alpine Fault or at certain elevations, and we explore the relative influence of different climate-mediated erosional processes on erosion.

5.1. Published and New Constraints on Rock-Uplift Rates and Topography

Our thermochronology-based exhumation estimates are shown graphically in Figure 1e. Interpolated exhumation rates calculated using only ZFT samples are generally greater than those calculated using only AFT samples (Figures S4b and S4c in Supporting Information S1). Given that most available samples (Table S2 in Supporting Information S1) are from these thermochronometric systems, Figure 1e essentially represents the average exhumation rates from ZFT and AFT (Figure S4d, Table S3 in Supporting Information S1). The data reveal that along the Western Southern Alps, exhumation rates are highest between the Karangarua and the Poerua catchments, locally peaking at ∼5–10 mm/yr around the Fox and Waiho catchments, and decay to the SW and NE (Figures 1e and 2c). This pattern generally agrees with published thermochronological studies (Batt et al., 2000; Herman et al., 2009; Jiao et al., 2018; Little et al., 2005; Tippett & Kamp, 1993a, 1993b). Topographic relief is highest in this central Western Southern Alps region with the fastest exhumation: mean elevations >1,500 masl and maximum elevations >2,500 masl only occur in the Fox and Waiho catchments (Figures 1c and 2a). Fault-throw rates along the Alpine Fault also reach their maximum of ∼10 mm/yr around the Fox-Waiho area, and decrease to the SW and NE, with the sharpest decrease at the intersection of the Hope Fault, the first fault of the Marlborough Fault System (Figures 1c and 2a). Mean catchment k_{sn} values show a similar pattern, with a maximum located where exhumation rates and fault-throw rates are highest, and decreasing values to the SW and NE, especially NE from the Hope Fault intersection (Figures 1d and 2b). In particular, mean catchment k_{sn} values correlate with the fault-throw rate at each catchment's outlet ($P < 0.001$, $R^2 = 0.56$; Figure 2d). k_{sn} also shows a general increase with exhumation rates, both for catchment-averaged values (Figure 2e), and for values extracted from a gridded k_{sn} map (Figure S4 in Supporting Information S1) for each thermochronology sample point (Figure 2e, inset). Overall, the available rock-uplift constraints and topographic proxies of rock-uplift (relief, k_{sn}) show general agreement. However, fault-throw rates are on average ∼4 times higher than the catchment-averaged exhumation rates (Figure 2f, Table 1).

5.2. New Catchment-Averaged Denudation Rates and Comparison With Rock-Uplift Rates, Their Geomorphic Expression, and Published Erosion Rates

Our new CRN denudation rates for the 19 major catchments between the Paringa and Maruia rivers and for one small frontal catchment mostly range between ∼0.6 and 9 mm/yr (Figure 1c). Only the Fox and Waiho catchments, with very low ^{10}Be concentrations (Table 2), may be denuding faster, but rate estimates for these catchments have very large uncertainties. Two other samples, our sample from the Waitaha and Larsen et al.'s (2014) Hokitika sample yielded denudation rates of ∼9 mm/yr from higher ^{10}Be concentrations, while having much lower uncertainties (Table 2 and Table S3 in Supporting Information S1). Hence, we infer that it is unlikely that denudation rates for the Fox and Waiho catchments are <9 mm/yr. Because uncertainties on the Fox and Waiho rates are too large to help constrain correlations with potential controlling parameters, they are excluded from any calculations but included in our plots for reference.

Our CRN denudation rates integrate over the last 275 yr on average, ranging from 67 yr for the Waitaha catchment to 958 yr for the Taramakau catchment (Table 1). Because enhanced sediment fluxes after major Alpine Fault earthquakes have been independently estimated to persist for ∼50–60 yr, and the last such earthquake was in 1717 CE (Howarth et al., 2014), our CRN denudation rates mostly represent inter-seismic erosion, except in catchments with relatively low denudation rates. The rates vary independently of catchment area (Figure S6a in Supporting Information S1, $P = 0.88$), indicating no systematic bias due to individual landslides or insufficient sediment mixing (Niemi et al., 2005; Yanites et al., 2009). Combining our data with published CRN concentrations from seven catchments (Larsen et al., 2014) yields a data set of 19 major catchments, with three repeated measurements that show good reproducibility. The data also include five tributary or small frontal catchments, of which the three catchments >2 km² are included in our analyses, and the two <2 km² are plotted only for reference (Figures 1c and 2a, Table S3 in Supporting Information S1).

CRN denudation rates, peaking in the central western Southern Alps and tapering to the NE and SW, with a sharp decline north of the intersection with the Hope Fault, follow the general pattern of exhumation rates, late Quaternary Alpine Fault throw rates, and catchment mean k_{sn} (Figures 2a–2c). CRN denudation rates show a good agreement with catchment mean k_{sn} ($P < 0.001$, $R^2 = 0.49$, Figure 3c), a proxy for rock uplift (Figures 2d and 2e) (Whipple et al., 1999). However, when compared directly, neither the fault-throw rates at the catchment outlets ($P = 0.03$, $R^2 = 0.25$; Figure 3a) nor the catchment-averaged exhumation rates ($P = 0.41$, $R^2 = 0.04$; Figure 3b) correlate well with the observed variability in CRN denudation rates. CRN denudation rates are generally lower than fault-throw rates (Figure 3a) and higher than catchment-averaged exhumation estimates (Figure 3b), but are generally within ±50% of these rock-uplift rate constraints (Table 1). Moreover, they are poorly correlated with other tectonic-influenced geomorphic variables, such as catchment relief or mean/maximum elevations ($P = 0.007–0.24$, $R^2 \sim 0.08–0.34$, Figures S5a–S5c in Supporting Information S1), mean slope ($P = 0.054$, $R^2 = 0.19$, Figures S5d and S5e in Supporting Information S1) or the proportion of catchment area steeper than the threshold hillslope angle of 32° for the Western Southern Alps (Clarke & Burbank, 2010) ($P = 0.06$, $R^2 = 0.19$, Figure S5f in Supporting Information S1).

To test whether suggested rock-uplift rate gradients perpendicular to the strike of the range influence CRN denudation rates, we examined whether erosion is enhanced at any distance from the Alpine Fault. We perform this test with the assumption that if rock-uplift rates were substantially greater either closer to the fault, at the main drainage divide, or halfway across the range, then catchments with a larger proportion of their drainage area within that particular distance-from-fault window (Figure S7a in Supporting Information S1) would experience faster denudation. A distance-from-fault window centered at ~11.5 km east of the fault, with a window size of ~12 km (i.e., ~6 to ~17 km east of the fault), is the one that best correlates with denudation rates (Figure S7b in Supporting Information S1). However, it only explains ~16% of the variability in our data set, and at a significance level of 1%, the null hypothesis that distance from the fault does not influence denudation rates cannot be rejected ($P = 0.075$, $R^2 = 0.16$, Figure S7c in Supporting Information S1). This finding further implies that the decrease in the metamorphic grade with distance from the Alpine Fault into the hanging wall also does not explain the variability in denudation rates well (Figure S1 in Supporting Information S1).

CRN denudation rates are ~25%–80% higher than erosion rates based on suspended sediment yields (Hicks et al., 2011), with which they show a somewhat systematic agreement ($P < 0.001$, $R^2 = 0.47$, Figure 3d, Table S3 in Supporting Information S1). Long-term landslide erosion rates below the tree line (Hovius et al., 1997) range from 5× higher to having values similar to our CRN denudation rates, with a median of 60% higher values for the long-term landslide erosion (Figure 3e, Table S3 in Supporting Information S1). However, landslide erosion rates averaged over 79 years (1935–2014) (Emberson et al., 2016) suggest that mass wasting below the treeline only accounts on average for ~10%–15% of the catchment-averaged ^{10}Be denudation rates over this time period (Figure 3f, Table S3 in Supporting Information S1). For the catchments that overlap with the landslide database (Paringa to Waitaha, Table S3 in Supporting Information S1), the mean integration timescale of the CRN data is ~128 years. While this longer timescale does not preclude the possibility that larger, less frequent landslides that occurred before 1935 add to the erosion captured by CRN data, the discrepancy between erosion estimates likely signals significant erosion by other processes, or at locations above the tree line.

5.3. Comparison of Catchment-Averaged Denudation Rates With Climate and Climate-Mediated Erosional Processes

We first compare our CRN denudation rates against the main climate and climate-mediated variables suggested to control erosion in the Western Southern Alps: precipitation and glacial cover. Differences in catchment-median annual precipitation ($P = 0.02$, $R^2 = 0.26$, Figure 4a) and median rainfall intensity (Figure S6c in Supporting Information S1), do not show significant corelations with CRN denudation rates. Only in three catchments do glaciers currently cover >15% of the catchment area, two of which are Fox and Waiho (excluded from our regressions) with 50% and 40% glacial coverage, respectively. Excluding Fox and Waiho, the average glacial cover for our studied catchments is <4% (including them, 7%), with more than half of the catchments having <1% glacial cover (Figures 1d and 2b, Table 1). We found a weak correlation between current glacial extent and CRN denudation rates ($P = 0.004$, $R^2 = 0.22$, Figure 4b). Glacier extents could have been ~100 m lower at the beginning of our average CRN integration timescale, ~275 years ago (Putnam et al., 2012) (see Study Area section, Figure S3a in Supporting Information S1). In that case, the average proportion of catchment area covered by glaciers
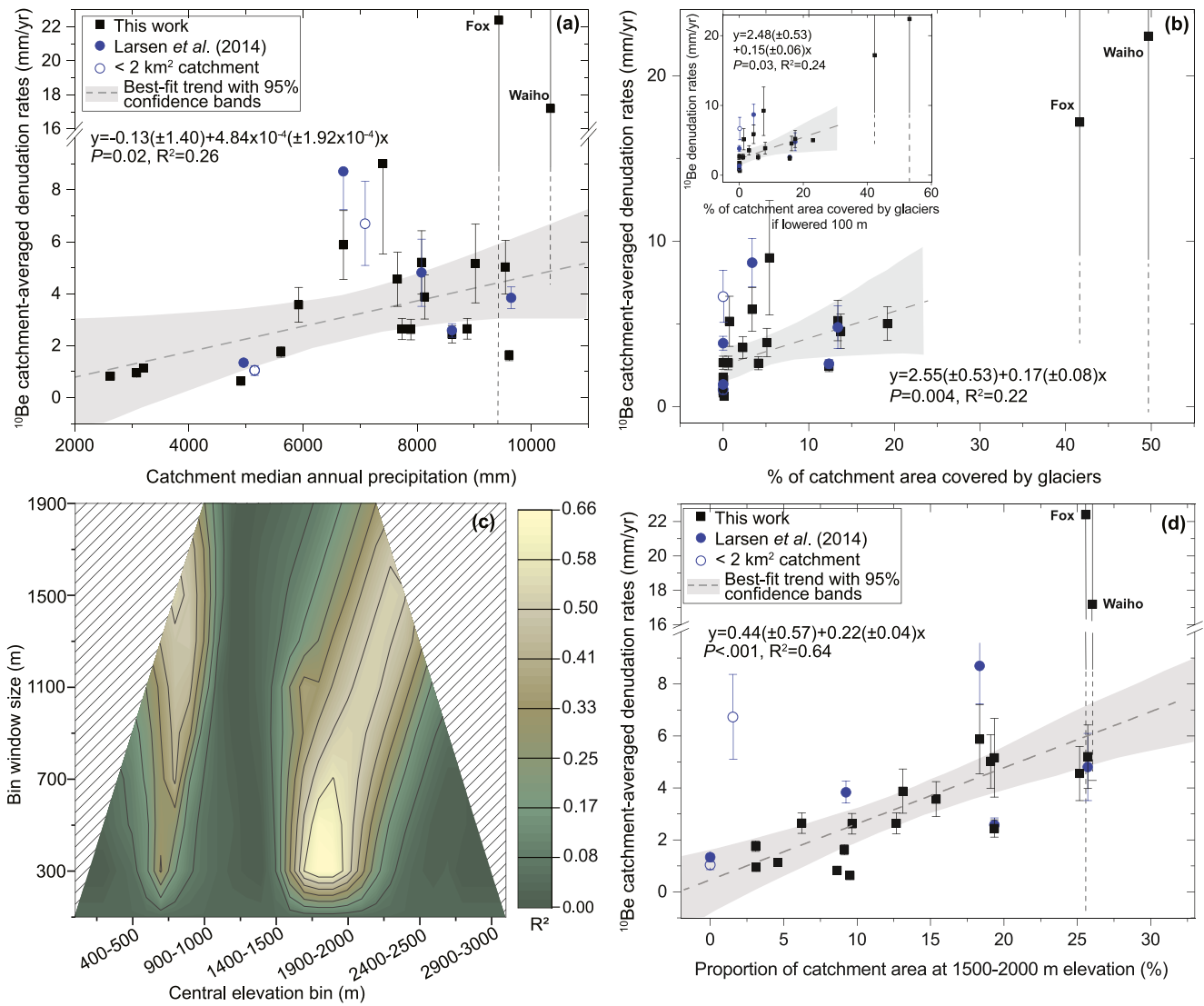
Figure 4. (a) Denudation rates against catchment-averaged median annual precipitation (MAP), derived from the 500 m × 500 m resolution rasters of MAP from NIWA, based on data from the period 1981–2010 (Figure S2 in Supporting Information S1). Details on the raw data acquisition and interpolation can be found in Tait et al. (2012). (b) Denudation rates against the proportion of catchment area currently covered by glaciers, and in the inset, the proportion of catchment area covered by glaciers if glaciers are lowered by 100 m elevation (i.e., their likely position at the beginning of the ^{10}Be average integration timescale). (c) Color map plot of the R^2 values that result from plotting denudation rates against elevation bins with different sizes (y) and central values (x). Hashed pattern represents combinations of (x) and (y) that are not possible given the catchment hypsometries. (d) Denudation rates versus % of catchment area in the 1,500–2,000 m elevation window.

would increase to 5% excluding Fox and Waiho, and 8% including them (Table 1). Glacial coverage per catchment would have been 0%–88% greater than current extents, with an average increase of 26% (Table 1). This extended glacier coverage affects the relationship between glacier coverage and denudation rates only marginally ($P = 0.03$, $R^2 = 0.24$, Figure 4b inset).

Using stepwise regression, we find that no combination of the variables examined so far explains denudation rates better than k_{sn} alone (Tables S5–S7, see Methods and extended methods in Supporting Information S1). Next, we examine whether erosion may be locally enhanced within the catchments at a certain elevation due to non-uniform precipitation or temperature. A potential for such enhancement is suggested by provenance studies (Jiao et al., 2018; Nibourel et al., 2015) and mapping of landslides (S. K. Allen et al., 2011) and scree distributions (Hales & Roering, 2005, 2009). In that case, we would expect that catchments with a larger proportion of their drainage area within a certain elevation window experience faster denudation. Three elevation windows correlate with denudation-rate variability substantially better than k_{sn}: Two with $R^2 = 0.66$ and $P < 0.001$, for

1,750 ± 150 masl and 1,850 ± 150 masl; and one with $R^2 = 0.64$ and $P < 0.001$, for 1,750 ± 250 masl (i.e., 1,500–2,000 masl) (Figure 4c and Figures S3c and S3d, Table S4 in Supporting Information S1). We note that the first two combinations are embedded in the latter, and the difference in the goodness-of-fit of the correlations are minimal, so we proceed with 1,500–2,000 masl as the preferred optimized elevation window (Figure 4d).

The 1,500–2,000 masl elevation window mostly coincides with the catchment and interfluve drainage divides and represents only 16% of the study area (Figures 5a and 5e). Although k_{sn} values are slightly higher for the 1,500–2,000 masl elevation range than lower-elevation windows (Figure 5b), only ~1% of the Western Southern Alps drainage network (considering a minimum flow accumulation threshold for fluvial channels of 2 km^2) is located at these elevations, comprising steep channel heads (Figures 1d, 5a, and 5b inset). Exhumation rates do not appear to be greater in this elevation range (Figure 5c), although to confirm this, a higher density of samples from high elevations would be needed (Figure 5c, inset). The 1,500–2,000 masl elevation window encompasses a wide range of distances from the Alpine Fault (Figure 5a, Figure S8 in Supporting Information S1), and is not characterized by a particular lithology, steeper slopes, or higher median annual precipitation (MAP) or rainfall intensity than the average for the Western Southern Alps (Figure S9 in Supporting Information S1). It is, however, characterized by a colder and narrower MAAT range compared to the whole study area (Figure S9d in Supporting Information S1).

While the majority of the Western Southern Alps is covered by forest (Figure 5d), in the 1,500–2,000 masl elevation range, 22% of the area is covered by glaciers, 77.4% by bare bedrock, and 0.5% by scrub vegetation (Figures 5d and 5f). Extending the currently mapped glaciers down by 100 m in elevation (assuming a +100 m isotherm shift in the last ~275 years, see Section 3.2) at the beginning of our average CRN integration timescale, glaciers would have covered 28.1% of the 1,500–2,000 masl elevation range (Figure S3a in Supporting Information S1, Figure 5f). The 1,500–2,000 masl elevation range is located between the hypsometric maxima of bare bedrock and glaciers (i.e., between the elevations with maximum bare bedrock and maximum glacial coverage), and just below the lowest estimated permafrost limit for the study area (Figure 5e). Thirty percent of the area in the 1,500–2,000 masl elevation window is within 100 horizontal meters of the nearest glacier, 50% within 300 m, and 80% within 1 km (Figure 6a). Although most of this elevation window is bare bedrock, the proportion of catchment area with bare bedrock does not correlate with denudation rate variability as well as the proportion of catchment area at 1,500–2,000 masl ($P = 0.02$, $R^2 = 0.26$, Figure 6a, inset).

5.4. The Interplay of Rock Uplift, Elevation, Climate, and Erosion

We next test if the elevation dependence of denudation rates reflects temperature dependence. To first order, frost-cracking is controlled by MAAT and annual temperature fluctuations (Andersen et al., 2015; R. S. Anderson et al., 2013; Hales & Roering, 2007; Rempel et al., 2016; Rengers et al., 2020), whereas deglaciation (and hence paraglacial erosion) is largely controlled by MAAT (Grämiger et al., 2017, 2020; Hugentobler et al., 2022). These climate-mediated erosional processes are also controlled by bedrock characteristics (R. S. Anderson et al., 2013; Hales & Roering, 2007; Hugentobler et al., 2022; Rempel et al., 2016). Since lithology and annual temperature fluctuations are relatively uniform across the Western Southern Alps (Figure S1a in Supporting Information S1, Hales & Roering, 2005, 2007, 2009), MAAT should be the main common parameter controlling variations in both peri- and paraglacial erosion.

We examined the potential influence of temperature-controlled erosional processes by plotting the distribution of MAAT values within each catchment, color-coded by the catchment-averaged denudation rate (Figure 6b). We consider the 0–4°C MAAT range as the most likely to host the frost-cracking and paraglacial adjustment window for the Western Southern Alps, based on published estimates (Hales & Roering, 2007, 2009). We find that catchments with MAAT distributions skewed toward lower temperatures, that is, with a greater proportion of their areas within the 0–4°C MAAT range, denude faster than those with MAAT distributions skewed toward higher temperatures (Figure 6b). The correlation of CRN denudation rates with the proportion of catchment area with 0–4°C MAAT ($P < 0.001$, $R^2 = 0.63$, Figure 6b inset) is much stronger than with the catchment-mean MAAT ($P = 0.007$, $R^2 = 0.34$, Figure S6b in Supporting Information S1).

To further test if elevation-dependent erosional processes play an important role in modulating denudation rates in the Western Southern Alps, we check if the residuals of the regressions of CRN denudation rates versus fault-throw rates (Figure 3a) and exhumation rates (Figure 3b) are well explained by the proportion of catchment area in the 1,500–2,000 masl window. We find that the proportion of catchment area in the peri- and paraglacial erosional
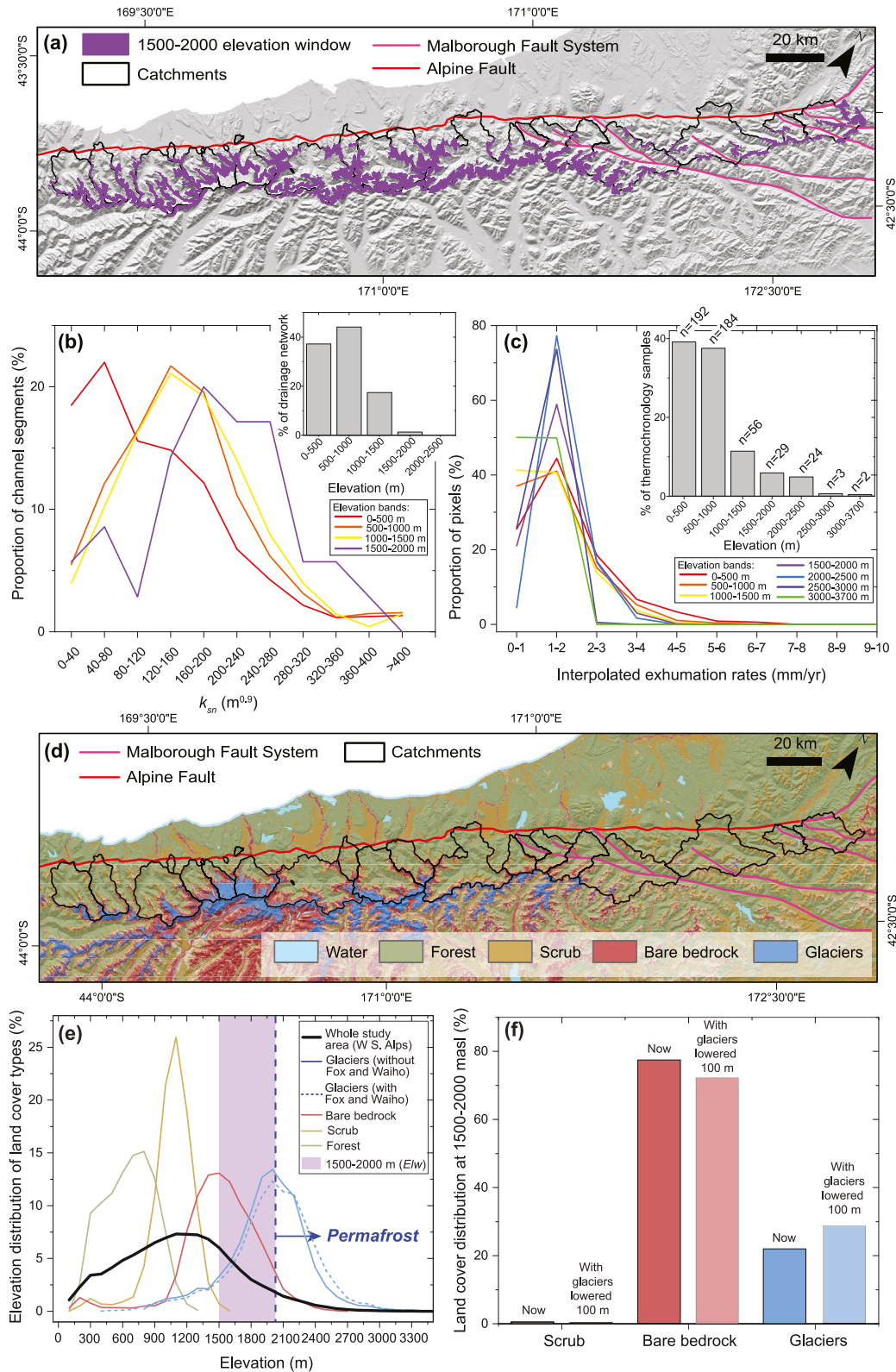
Figure 5.

window explains ≥60% of the scatter in the relation between denudation rates and throw rates ($P < 0.001$, $R^2 = 0.66$; Figure 6c) and exhumation rates ($P < 0.001$, $R^2 = 0.60$; Figure 6d). This result suggests that processes occurring at these elevations modulate the tectonic control on denudation and can amplify or reduce denudation rates by a few mm/yr (Figures 6a and 6b, Table 1). We find an almost identical result if the proportion of catchment area with 0–4°C MAAT is used instead of the 1,500–2,000 masl window (Figure S10 in Supporting Information S1).

In all mountain regions, MAAT is dictated by elevation, so it is at least partially controlled by rock-uplift rates. We find that as rock-uplift rates (here represented by k_{sn}, as it scales both with throw rates and exhumation rates, Figures 2d and 2e) increase, the proportion of the catchment area within the elevation window that hosts peri- and paraglacial erosion (below referred to as the *PPPEw*) increases, resulting in faster catchment-averaged denudation (Figure 7). Stepwise regression analyses reveal that a linear model including only *PPPEw* as an independent variable performs as well as a model including both k_{sn} and *PPPEw* as independent variables (see Methods and Table S6 in Supporting Information S1). In other words, k_{sn} (i.e., tectonics) becomes redundant when combined with *PPPEw*, probably because *PPPEw* already embeds an underlying tectonic control (Figure 7).

6. Discussion

6.1. Insights Into Rock-Uplift Distribution

CRN denudation rates are within the same order of magnitude, and generally within ±50%, of fault-throw rates (Figures 2a and 3a) and thermochronology-derived exhumation rates (Figures 1e, 2c, and 3b) and show a reasonably good correlation with k_{sn} (Figure 3c). This finding suggests that tectonics is the first-order control on denudation, and that the Western Southern Alps landscape is close to an erosional steady state, as first suggested by Adams (1980). Our CRN denudation rates are generally lower than Holocene Alpine Fault throw rates (Figures 2a and 3a), probably because our data mainly capture inter-seismic erosion, while throw rates integrate over several seismic cycles (Norris & Cooper, 2001). Fault-throw rates that capture rock-uplift at the fault are greater than catchment-averaged exhumation rates (Figure 2f, Table 1), possibly because exhumation is likely fastest close to the Alpine Fault (Figure 1e), and hence exhumation averaged over entire catchments may be inherently lower.

Our analyses also provide insights into the spatial distribution of rock-uplift rates along the range. Our denudation rates show that the zone of extremely fast erosion (>9 mm/yr) is limited to the Fox and Waiho catchments (Figure 2a), supporting the conclusions of a thermochronological study that infers that this narrow sector is affected by a restraining bend that locally generates extremely fast rock uplift (Little et al., 2005) (Figures 1e and 2c). The distribution of CRN denudation rates and k_{sn} values along the Alpine Fault (Figures 2a and 2b) also support previous observations, based on late Quaternary throw rates, of a sharp decrease in rock-uplift rates north of the intersection of the Hope Fault, likely due to slip redistribution onto the Marlborough Fault System (Figure 1c) (Norris & Cooper, 2001).

Our findings of a lack of a strong distance-from-fault control on denudation rates (Figure S7 in Supporting Information S1) are not consistent with studies suggesting that rock uplift is fastest either at the main drainage divide (Beavan et al., 2010), halfway across the range (Adams, 1980), or closer to the Alpine Fault (Batt et al., 2000; Herman et al., 2009; Little et al., 2005; Tippett & Kamp, 1993a, 1993b). Our results also differ from a provenance study suggesting enhanced erosion ~11 km SE of the Alpine Fault (Nibourel et al., 2015). The apparent disagreements may arise because: (a) across-range rock-uplift patterns may not be uniform along the length of the Western Southern Alps, and the studies were conducted in different sectors along strike; (b) the studies integrate over different timescales (e.g., ≤10^1 yr for the GPS-based study, Beavan et al., 2010); ~10^2 yr for our CRN study; >10^3 yr for the terrace-based study (Adams, 1980); 10^6 yr for the thermochronological studies (Batt

Figure 5. (a) Location in the map of the 1,500–2,000 masl elevation window. (b) Distribution of k_{sn} values of channel segments for different elevation bands, extracted from Figure 1d. The inset shows the proportion of the total drainage network that falls in each elevation band. (c) Distribution of exhumation rate values for different elevation bands, extracted from Figure 1e. The inset shows the number of thermochronological samples (Figure 1e) that are located in each elevation band. (d) Distribution of current land cover types from the EcoSat landcover map derived from Landsat 15 m × 15 m resolution imagery by New Zealand Landcare Research. Details on the methods applied to Landsat imagery to classify land cover can be found in Dymond and Shepherd (2004a, 2004b). (e) Hypsometry of different types of land cover for the Western Southern Alps study area. The dashed vertical dark blue line marks the lower limit of permafrost on the study area (S. K. Allen et al., 2009; Sattler et al., 2016), with the blue arrow pointing at the elevation range likely affected by permafrost. (f) Distribution of types of land cover in the 1,500–2,000 masl elevation window, for the current cover extents, and for the scenario with 100 m lower glaciers (likely conditions at the beginning of our average ^{10}Be integration timescale ~275 years ago).
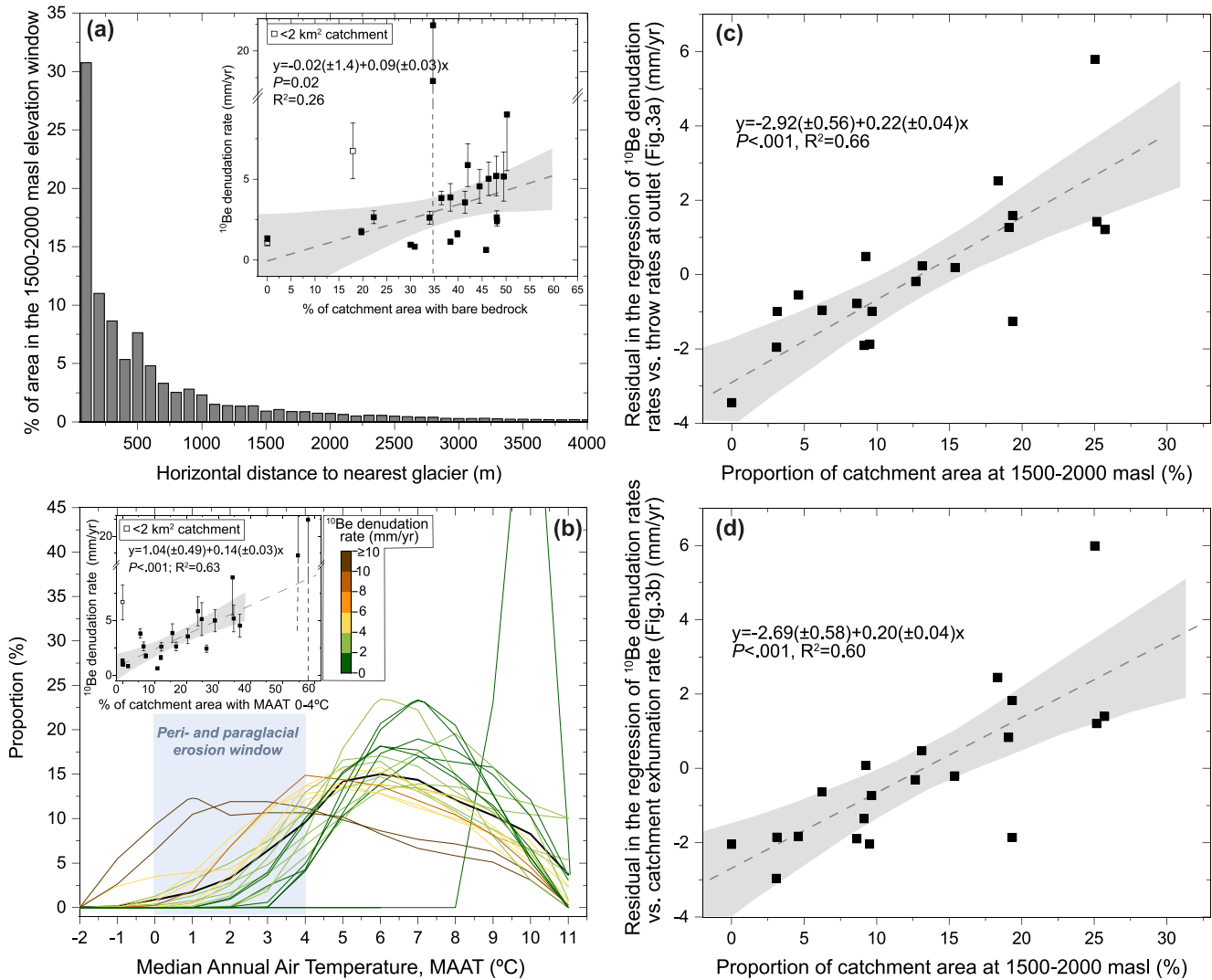
Figure 6. (a) Distribution of horizontal distance to nearest glacier for the area within the 1,500–2,000 masl elevation window. The inset shows ^{10}Be denudation rates plotted against the proportion of catchment area with bare bedrock (Table 1). (b) Distribution of median annual air temperatures (MAAT) for each catchment, color-coded by catchment-averaged denudation rate. MAAT is derived from the 500 m × 500 m resolution rasters of median annual temperature from NIWA, based on data from the period 1981–2010 (Figure S2 in Supporting Information S1). Details on the raw data acquisition and interpolation can be found in Tait and Macara (2014). The inset shows denudation rates versus the proportion of catchment area with MAAT between 0 and 4°C (the window of peri- and paraglacial erosion for the study area). The thick black line corresponds to the elevation distribution of all Western Southern Alps catchments combined. Residuals from the regressions of ^{10}Be denudation rates versus throw rates at catchment outlets (Figure 3a) and versus catchment-averaged exhumation rates (Figure 3b) plotted against the proportion of catchment area at 1,500–2,000 masl, in (c) and (d), respectively. Equivalent graphs plotted against the proportion of catchment area with MAAT between 0 and 4°C are shown in Figure S10 in Supporting Information S1.

et al., 2000; Herman et al., 2009; Little et al., 2005; Tippett & Kamp, 1993a, 1993b), and different rock-uplift patterns may dominate over different timescales; and/or (c) the spatial patterns of denudation and rock uplift may be decoupled if variables other than rock uplift modulate the connection between tectonics and erosion. Indeed, the relatively good correlation between denudation rates and k_{sn} (Figure 3c) but weaker correlation with throw rates (Figure 3a), exhumation rates (Figure 3b), relief and mean/maximum elevation (Figure S5 in Supporting Information S1), may indicate that processes other than tectonics also influence erosion and mountain topography in the Western Southern Alps.
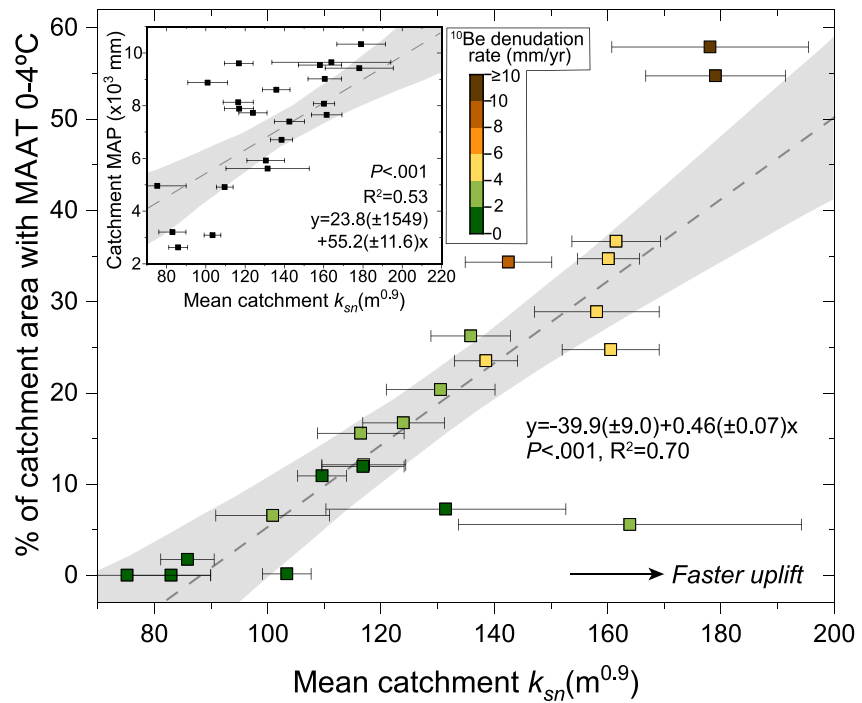
Figure 7. Proportion of catchment area with median annual air temperatures (MAAT) between 0 and 4°C, and catchment median annual precipitation (MAP, inset) plotted against k_{sn}, proxy for uplift rates, color-coded by catchment denudation rate.

6.2. Erosional Processes Driving Elevation-Dependent Denudation and Their Links to Tectonics

Our findings suggest that catchment-averaged denudation rates are modulated by elevation-dependent erosional processes (Figures 4c and 4d), preferentially occurring at bare bedrock slopes and ridges in the 1,500–2,000 masl elevation range (Figures 5 and 6a), and potentially influenced by temperature (Figure 6b). We suggest that the proportion of catchment area at 1,500–2,000 masl is the variable that best correlates with denudation rates because this variable partially embeds tectonic information (Figure 7): rock uplift is the main mechanism creating mountain relief that can reach elevations >1,500 masl (Figures 2a–2c), and hence it exerts an underlying primary control on denudation rates. Moreover, bedrock in ridges (where most of the 1,500–2,000 masl window is located, Figure 5a) has been subjected to uplift for longer than bedrock in valleys, and has less confining support, possibly facilitating other erosional processes. However, this tectonic control appears modulated by elevation-dependent, likely temperature-mediated, erosional processes, which explain denudation-rate variability (Figures 4c, 4d, and 6b) and the residuals in denudation versus rock-uplift regressions (Figures 6c and 6d) better than any other variable (Table S6 in Supporting Information S1), and 15% better than k_{sn}. There is no evidence for rock-uplift rates being greater at the 1,500–2,000 masl elevation range, although more thermochronological data from high elevations are needed to test this hypothesis (Figure 5c). Likewise, the potential contribution of advection to enhanced erosion on bedrock ridges, and the role that increased ridge erosion may play in drainage divide mobility (Castelltort et al., 2012) should be investigated in the future.

The Fox and Waiho catchments are still clearly dominated by glacial erosional processes (Table 1, Figures 1d, 2b, and 4b). But for other catchments, and in the 1,500–2,000 masl elevation window, glacier coverage is low (Table 1, Figures 1d, 2b, and 4b). Hence, we infer that glacial scour is unlikely to be the main erosional process behind the observed elevation/temperature dependent erosional patterns. Instead, our data suggest that the local-ized zone of enhanced erosion coincides with the elevation range that has recently experienced or is currently experiencing glacier retreat (S. K. Allen et al., 2009, 2011; Sattler et al., 2016), with most of the 1,500–2,000 masl window being within 1 km of the nearest receding glacier (Figures 5d–5f and 6a). This is the elevation range where paraglacial erosional processes are expected to be most active. In the Western Southern Alps, these elevations also correspond to locations that could have experienced permafrost thawing since the LIA or that host currently degrading permafrost (S. K. Allen et al., 2009, 2011; Sattler et al., 2016). Indeed, enhanced land-

sliding has been reported at these elevations and is attributed to paraglacial hillslope adjustment and permafrost degradation (S. K. Allen et al., 2009, 2011). In landslide-prone settings such as the Western Southern Alps, rapid rock uplift is always necessary to maintain steep slopes and continued landsliding, and it can be challenging to unambiguously attribute landsliding to paraglacial erosion. However, the spatial and temporal patterns of landsliding with respect to retreating glaciers link landslide activity to paraglacial adjustment (S. K. Allen et al., 2009, 2011; Cody et al., 2020). Erosion peaking at 1,500–2,000 masl is also consistent with a provenance study that found that during the Holocene, most sediment is sourced from high-elevation, recently deglaciated areas (Jiao et al., 2018). Given that the 1,500–2,000 m elevation window mostly contains bare bedrock ridges and hillslopes (Figure 5a), and that the Western Southern Alps have little moraine material preserved (Barrell, 2011) relative to its high sediment fluxes, paraglacial sediment evacuation from moraines is unlikely to be a significant contributor to our estimated catchment denudation rates.

The 1,500–2,000 masl elevation window of maximum denudation in the Western Southern Alps is strikingly similar to the 1,550–2,000 masl elevation window suggested to host the most intense frost-cracking on the range (Hales & Roering, 2007). Therefore, we infer that periglacial erosional processes may be an important contributor to denudation by modulating physical erosion rates on both sides of the Southern Alps. In support of this interpretation, denudation rates seem controlled by a narrow range of elevations (Figures 4c and 4d), and thus temperatures (Figure 6b) rather than simply scaling with mean/maximum elevations (Figures S5b and S5c in Supporting Information S1) or with catchment-mean MAAT (Figures S6b in Supporting Information S1). If denudation rates increased (Draebing et al., 2022) or decreased (Lehmann et al., 2020) monotonically with elevation, as reported in the European Alps, the correlation between denudation rate and catchment mean and maximum elevations should be stronger than in our findings (Figures S5a–S5c in Supporting Information S1). Our observations are in agreement with findings from Rengers et al. (2020), who measured greater frost-cracking-derived sediment production at times of lower Mean Air Temperatures, which coincided with times where rock surfaces spent more hours in the frost-cracking window, and with greater depth-integrated frost-cracking intensities. Low scree coverage in the Western Southern Alps compared to the eastern Southern Alps was thought to indicate that frost-cracking is less important than landsliding as an erosional process (Hales & Roering, 2005, 2009). However, differences in mapped scree between the eastern and western Southern Alps could relate to differences in preservation potential of the scree, considering the contrasting MAP across the range (Figure 1b and Figure S32b in Supporting Information S1). Nevertheless, abundant scree, potentially frost-cracking-derived, can be observed in many parts of the Western Southern Alps at 1,500–2,000 masl (Figure S12 in Supporting Information S1). Landslides sourced from hilltops can also be commonly found at these elevations (Figure S12 in Supporting Information S1). These observations document intense peri- and paraglacial processes occurring in the 1,500–2,000 masl elevation window, although in detail the exact elevation range of enhanced erosion may vary throughout the study area due to factors such as hillslope aspect or slope, which affect snow and regolith cover and insulation.

Headwall-denudation rates on frost-cracking-dominated hillslopes of the eastern Southern Alps have been estimated to be <1 mm/yr (Hales & Roering, 2009). In contrast, in the Western Southern Alps: (a) faster rock uplift supplies fresh bedrock at a faster rate; (b) bedrock is more pervasively fractured (Clarke & Burbank, 2010), potentially enhancing frost-cracking activity; and (c) steeper slopes (Clarke & Burbank, 2010) and greater MAP could facilitate a more efficient removal of scree, minimizing the accumulation of insulating regolith and efficiently connecting zones of scree production with the fluvial system. Consequently, frost cracking in the Western Southern Alps may facilitate faster denudation compared with the eastern Southern Alps. Moreover, due to the paucity of insulating scree, frost cracking in the Western Southern Alps could penetrate to depths up to ~2.2 m (Hales & Roering, 2007), conditioning the bedrock for mass wasting and potentially enhancing paraglacial landsliding. The presence of bare bedrock in itself correlates only weakly with denudation rates (Figure 6a, inset), indicating that bedrock exposure and lack of vegetation cohesion are, on their own, insufficient to drive the observed enhanced erosion. Instead, the lack of vegetation at these elevations (Figures 5d and 5f) likely amplifies thermal stresses and further facilitates frost cracking (Andersen et al., 2015; Collins & Stock, 2016). Pervasive bedrock fracturing on its own is also unlikely to generate rapid erosion: although available bedrock fracturing surveys (Clarke & Burbank, 2010) do not have the resolution to resolve fracture gradients across the Western Southern Alps, bedrock is expected to be more fractured closer to the Alpine Fault, where our data do not support enhanced erosion (Figure S7 in Supporting Information S1). Moreover, if slopes are adjusted to differences in erodibility, we would not necessarily expect bedrock fracturing differences to result in differences in erosion rate.

We also note that temperature-dependent processes that are effective at 1,500–2,000 masl are not sufficient on their own to drive enhanced erosion. Steep slopes and rapid rock uplift, both generated by tectonic activity, are required to facilitate sediment evacuation and ensure continuous bedrock exposure. This interpretation is supported by the lower denudation rates in the Eastern Southern Alps (despite having more surface area located at 1,500–2,000 masl; Hales & Roering, 2005, 2009), and by ^{10}Be denudation rates from the Gunn Ridge north-draining tributary (Larsen et al., 2023). This small tributary (<0.5 km^2) of the Whataroa catchment has 52% of its drainage area at 1,500–2,000 masl (Figure S13 in Supporting Information S1, not included in Figure 1 given its very small size), but a ^{10}Be denudation rate of only 0.89 mm/yr (as reported by Larsen et al., 2023; equivalent to 0.80 mm/yr using the same parameters as for our samples). This rate is more in line with the ^{10}Be denudation rates from frost-cracking-dominated hillslopes of the Eastern Southern Alps (0.30–0.86 mm/yr; Hales & Roering, 2009), and with soil denudation rates from the Western Southern Alps (Larsen et al., 2014, 2023). We propose that the low ^{10}Be denudation rate of the Gunn ridge north-draining tributary could be due to its relatively low mean slope (mean slope of 23°, in contrast with 29° for the 1,500–2,000 masl window throughout the study region), low relief (338 m), very small drainage area, and disconnection from the fluvial system (it is a relict glacial hanging valley), which mean that scree is not efficiently evacuated. Inefficient scree removal is consistent with aerial imagery observations, which show abundant vegetated scree on the hillslopes of this tributary (Figure S13 in Supporting Information S1).

To summarize, our results suggest that elevation-dependent erosion in the Western Southern Alps, with a maximum at 1,500–2,000 masl, is probably driven by the combined action of temperature-controlled peri- and paraglacial erosional processes, superimposed on the primary tectonic control that generates relief at these elevations, steep slopes, and ensures rapid supply of bedrock. Ultimately, this interpretation should be verified by collecting ^{10}Be catchment-averaged denudation rate samples for nested catchments at different elevations and for catchments with different mean slopes. Although rock uplift is the primary variable controlling erosion, it is not an erosional process per se; it requires the intervention of erosional processes to exert its control. In doing so, other factors, such as climate, may become secondary modulators of erosion over <10^6 yr timescales by amplifying or decreasing the rates dictated by rock uplift through different erosional processes that are active at particular times of glacial-interglacial cycles.

Over the last 10^1–10^2 years captured by our CRN data, the link between rock uplift and erosion in the Western Southern Alps seems to be mediated by temperature-controlled processes, which modulate the underlying tectonic control on erosion (Figures 6c and 6d) and explain denudation-rate variability better than rock-uplift alone (Figures 4c, 4d, and 6b; Table S7 in Supporting Information S1). We propose that the proportion of catchment area at 1,500–2,000 masl explains denudation rate variability 15% better than k_{sn} (Figures 3c and 4d) because this first variable embeds both tectonic information (like k_{sn} does), and the influence of temperature-controlled erosional processes. Surprisingly, we find that temperature seems to be a more important climate variable in explaining denudation rate variability than precipitation in the Western Southern Alps (Figures 4a and 6b), and it has a clearer link with tectonics than precipitation (Figure 7), contrasting with common assumptions (Whipple, 2009). The dominant role of temperature is likely enabled in the Western Southern Alps by the high precipitation rates throughout the landscape, which mean that most sediment produced is efficiently transported, producing a dominantly detachment-limited landscape (i.e., bedrock-dominated).

6.3. Implications of Fast Denudation Rates Facilitated by Peri- and Paraglacial Processes, and the Role of Temperature Modulating Erosion

Both trends in Figures 6c and 6d suggest that catchments with <13% of their areas in the 1,500–2,000 masl elevation range have lower denudation rates than would be expected given their rock-uplift rates, while catchments with >13% of their areas in that elevation range have higher denudation rates than predicted by rock-uplift, by a range of values of more than ±3 mm/yr (Table 1). Therefore, our data suggest that peri- and paraglacial processes can significantly modulate catchment-averaged denudation rates and induce erosion rates of >2 mm/yr, balancing some of the highest sustained rock-uplift rates on Earth (Figures 1e, 2a, and 2c). To our knowledge, previous catchment-averaged denudation rates attributed to peri- or paraglacial bedrock erosion are <2 mm/yr, with spatial or temporal denudation-rate differences within a factor of 3 (Delunel et al., 2010; Marshall et al., 2015). Most rockwall erosion-rate estimates related to peri- and paraglacial erosion are also <2 mm/yr (Draebing et al., 2022; Elkadi et al., 2022; Hartmeyer et al., 2020b). The only exceptions are a few faster estimates derived from single rockwalls over periods of a few years (Draebing et al., 2022), which may not be representative of landscape-scale

erosion over longer timescales. Hence, our data substantially expand the observed range of the rates that these erosional processes can attain at catchment and orogen scales (Delunel et al., 2010; Draebing et al., 2022; Hartmeyer, et al., 2020b; Marshall et al., 2015). Moreover, the decrease or increase in denudation rates that could be attributed to climate (i.e., the values of the residuals from rock-uplift metrics plotted in Figures 6c and 6d) represents on average ∼70%–80% (median of ∼40%) of the denudation rate values. This implies that over 10^1–10^2 timescales, the link between erosion and rock uplift can be modulated by the climate by ∼40%–80%.

The apparent importance of peri- and paraglacial erosion in a rapidly uplifting area implies that these processes could be as effective as glaciers or coupled river incision and landsliding as erosional agents, and thus contribute to limiting mountain elevations, supporting the "periglacial buzzsaw" hypothesis (Egholm et al., 2015; Hales & Roering, 2009). The hypsometric maximum of the Western Southern Alps, with a wide peak between 900 and 1,400 masl, is located between the estimated Equilibrium Line Altitude at the LGM at ∼900 masl (Tielidze et al., 2022) and the current lower limit of the peri- and paraglacial erosion window (1,500–2,000 masl) (Figure 5e). The concentration of intense para- and periglacial erosion at 1,500–2,000 m during the Holocene, and likely at lower elevations during glacial periods, could have contributed to sustaining modal elevations <1,400 m, well below current snowlines (Figures 5a, 5d, and 5e), even in one of the fastest-uplifting mountain ranges on Earth. Future studies could test this hypothesis using a landscape evolution model. When integrated over the past 25 kyr based on climate records, maximum cumulative frost-cracking intensity for the Southern Alps was estimated to be between 2000 and 2,500 masl (Hales & Roering, 2007). This finding was used by Hales and Roering (2007) to support the periglacial buzzsaw hypothesis on the eastern Southern Alps, where peak elevations are relatively constant at ∼2,000 m. However, these authors argued that close to the main drainage divide, periglacial erosion rates are not sufficient to balance rapid rock-uplift. Our new data suggest that this inefficiency may only be the case for the narrow central sector of the range where rock-uplift rates exceed 9 mm/yr. Elsewhere in the Western Southern Alps, peri-, and paraglacial erosion appear to modulate erosion rates by up to 2–3 mm/yr (∼40%–80% of the total denudation rate). Hence, these processes could contribute to limiting mountain elevations during times when their window of activity covers a significant surface area on the range.

6.4. Implications for the Timescale of Erosional Adjustment in Response to Changing Temperatures

Both ice segregation modeling, based on modern temperature records (20–100 years; Hales & Roering, 2007), and our CRN data indicate enhanced denudation at ∼1,500–2,000 masl (i.e., 1,750 ± 250 m) in the Southern Alps. The likely vertical isotherm shift of +100 m during the ∼275 yr average integration timescale of our denudation rates (Kaplan et al., 2013; Putnam et al., 2012) (see Study Area section in Supporting Information S1) represents only 20% of the 500-m-wide window of enhanced denudation. Lowering the elevation window by 100 m to reproduce the colder conditions ∼275 years ago (and using the same bin window sizes that provided best fits in Figure 4c, of ±150 and ±250 m, Table S4 in Supporting Information S1) yields worse, but still reasonable correlations with denudation rates: $R^2 = 0.59$ and $P < 0.001$ for 1,500–1,800 masl (1,650 ± 150 m); $R^2 = 0.52$ and $P < 0.001$ for 1,400–1,900 masl (1,650 ± 250 m) (Figure 4c, Figures S14a and S14b, Table S4 in Supporting Information S1). Moreover, the relative temperature differences across catchments (Figure 6b) likely remained similar during the CRN integration timescale. These findings suggest that the most intense erosion may have occurred within a similar (±100 m) elevation window for the last ∼275 years.

Our CRN data mostly cover the time period after the LIA. Lowering the central value of our enhanced denudation window by 200 m to simulate LIA conditions produces substantially worse fits to our data ($R^2 = 0.32$ and $P = 0.009$ for a window at 1,300–1,800 masl, i.e., 1,550 ± 250 masl; and $R^2 = 0.35$ and $P = 0.006$ for 1,400–1,700 m, i.e., 1,550 ± 150 masl; Figure 4c, Figures S14c and S14d, Table S4 in Supporting Information S1). Thus, our CRN data appear to reflect a fast denudational response, on a decadal to centennial timescale, to warming following the end of the LIA peak, and a slower upward migration of the enhanced erosional window for the last ∼275 years. This fast erosional response is consistent with recent work in Fox valley that shows slope failures starting during the last stages of glacier retreat or very shortly after (within years) (Cody et al., 2020). This rapid hillslope response is in agreement with recent data from Alaska (Williams & Koppes, 2019) and from the European Alps (Draebing et al., 2022) that suggest adjustment on decadal timescales. However, it differs from the earlier notion that paraglacial adjustment occurs on millennial timescales (Grämiger et al., 2017).

For the Western Southern Alps, a fast erosional response is likely due to efficient peri- and paraglacial erosion facilitated by rapid rock-uplift rates (Figures 1e, 2a, and 2c), the lack of vegetation at relevant elevations (Figures 5d–5f), and efficient removal of eroded material driven by high precipitation rates (Figure S2b in

Supporting Information S1). This apparent fast response of the Western Southern Alps to climatic perturbations (Prasicek et al., 2015) may presage an upward shift in the elevation distribution of erosion in response to ongoing rapid warming in other alpine landscapes worldwide. For orogens with less surface area at elevations higher than the current peri- and paraglacial erosional windows, this may result in a decrease in catchment denudation rates.

6.5. Implications of Enhanced Erosion Above the Tree Line

Our results imply that previous studies focusing on erosion below the tree line (∼1,400 m; Hovius et al., 1997; Emberson et al., 2016; Wang et al., 2020) may only capture a limited proportion of total erosion in the Western Southern Alps. Landslide erosion rates averaged over decadal timescales (1935–2014, 79 years) from below the tree line (Emberson et al., 2016) are substantially lower than our catchment-averaged CRN denudation rates, allowing for 85%–90% of the total erosion to occur above the treeline on this time scale (Table S3 in Supporting Information S1). Moreover, our rates and inferred locus of erosion are inconsistent with estimated long-term landslide erosion rates below the treeline (Hovius et al., 1997), which are ∼60% higher than our CRN catchment-averaged denudation rates. Although the long-term landslide-erosion estimates could change if the longer observation interval of 1935–2014 from Emberson et al. (2016), and a regional area-volume scaling would be considered, the inconsistency is likely linked to the differing averaging timescales of these two approaches. Long-term landslide erosion rates include rare, very large events, which, according to observed area-volume and size-frequency scaling of landslides, dominate the erosion budget (cf. Marc et al., 2019). In the Western Southern Alps, the return time of such landslides exceeds the integration time of CRN denudation rates, causing a decoupling of CRN rates from the process that may determine erosion rates on millennial time scales. Hence, we posit that enhanced erosion at 1,500–2,000 masl does not reflect the long-term erosional pattern, but it is likely a transient feature that is dictated by changing climate and glacial retreat. Even if peri- and paraglacial erosion have strongly modulated denudation rates over the last several decades to centuries, with climate cycles continuously shifting the zones of enhanced erosion, on million-year timescales, assuming no major changes in topography, catchment-averaged denudation rates are expected to match catchment-averaged rock-uplift rates.

7. Conclusions

We present 20 new ^{10}Be catchment-averaged denudation rates from all major catchments of the Western Southern Alps of New Zealand. Denudation rates are generally between 0.6 and 9 mm/yr, and within the same order of magnitude as rock-uplift rates. This similarity between denudation and rock-uplift rates, together with denudation rates showing a reasonable correlation with k_{sn}, reflects the dominant control of tectonics on erosion rates. However, we find that the proportion of catchment area in the 1,500–2,000 masl elevation range correlates with denudation rates better than any other variable, and 15% better than the correlation with k_{sn}, while also explaining ∼60% of the deviation of denudation rates from rock-uplift rates. We propose that this strong predictive power arises because the proportion of catchment area at 1,500–2,000 masl embeds both tectonic information (necessary to create relief at those elevations in the first place), and the influence of temperature-controlled erosional processes. We infer that temperature-controlled periglacial and paraglacial erosional processes are acting as important modulators of denudation over 10^1–10^2 yr timescales, transiently enhancing erosion in the 1,500–2,000 masl elevation range and amplifying or decreasing the erosion rates dictated by rock uplift by up to ±3 mm/yr. Efficient periglacial and paraglacial erosion likely relies on steep slopes and high precipitation rates that ensure effective sediment evacuation. We find that the relationships among temperature, rock uplift, and erosion are stronger than those among precipitation, rock uplift, and erosion, indicating that links between tectonics and climate are in some cases dominated by temperature- rather than rainfall-driven erosion. This finding brings into question the common assumption, typically incorporated into landscape-evolution models, that tectonic-climate-topographic interactions only occur through erosion driven by precipitation or glaciation. The importance of temperature-dependent erosional processes in rapidly uplifting mountain belts could have implications for physico-chemical erosional feedbacks, and raise crucial questions regarding changes in the pattern and rates of erosion in warming/cooling climates and their feedback with atmospheric CO_2 concentrations.

Conflict of Interest

The authors declare no conflicts of interest relevant to this study.

Data Availability Statement

The raster with suspended sediment yields is available for download from Shankar and Hicks (2002), and rasters of median annual temperatures and median annual precipitation are available at Tait and Zheng (2007). The 1:250000 Geological Map of New Zealand can be downloaded from the GNS Science (New Zealand's Institute of Geological and Nuclear Sciences) website at GNS Science (2014). The EcoSat landcover map, by New Zealand Landcare Research, can be downloaded from Dymond and Shepherd (2004a). The Matlab script used to find the optimal distance-from-fault and elevation windows, the shapefiles of catchment outlines, raw CRN data, and compilations of themochronometric cooling ages can be downloaded from Roda-Boluda (2023).

References

Adams, J. (1980). Contemporary uplift and erosion of the Southern Alps, New Zealand. *GSA Bulletin*, *91*(1_Part_II), 1–114. https://doi.org/10.1130/gsab-p2-91-1

Allen, P. A., Armitage, J. J., Whittaker, A. C., Michael, N. A., Roda-Boluda, D., & D'Arcy, M. (2015). Fragmentation model of the grain size mix of sediment supplied to basins. *The Journal of Geology*, *123*(5), 405–427. https://doi.org/10.1086/683113

Allen, S. K., Cox, S. C., & Owens, I. F. (2011). Rock avalanches and other landslides in the central Southern Alps of New Zealand: A regional study considering possible climate change impacts. *Landslides*, *8*(1), 33–48. https://doi.org/10.1007/s10346-010-0222-z

Allen, S. K., Gruber, S., & Owens, I. (2009). Exploring steep bedrock permafrost and its relationship with recent slope failures in the Southern Alps of New Zealand. *Permafrost and Periglacial Processes*, *20*(4), 345–356. https://doi.org/10.1002/ppp.658

Andersen, J. L., Egholm, D. L., Knudsen, M., Jansen, J. D., & Nielsen, S. (2015). The periglacial engine of mountain erosion—Part 1: Rates of frost cracking and frost creep. *Earth Surface Dynamics*, *3*(4), 447–462. https://doi.org/10.5194/esurf-3-447-2015

Anderson, B., & Mackintosh, A. (2006). Temperature change is the major driver of late-glacial and Holocene glacier fluctuations in New Zealand. *Geology*, *34*(2), 121–124. https://doi.org/10.1130/g22151.1

Anderson, R. S. (1998). Near-surface thermal profiles in alpine bedrock: Implications for the frost weathering of rock. *Arctic and Alpine Research*, *30*(4), 362–372. https://doi.org/10.2307/1552008

Anderson, R. S., Anderson, S. P., & Tucker, G. E. (2013). Rock damage and regolith transport by frost: An example of climate modulation of the geomorphology of the critical zone. *Earth Surface Processes and Landforms*, *38*(3), 299–316. https://doi.org/10.1002/esp.3330

Barrell, D. (2011). Quaternary glaciers of New Zealand. In *Developments in quaternary sciences* (Vol. 15, pp. 1047–1064). Elsevier.

Batt, G. E., Braun, J., Kohn, B. P., & McDougall, I. (2000). Thermochronological analysis of the dynamics of the Southern Alps, New Zealand. *Geological Society of America Bulletin*, *112*(2), 250–266. https://doi.org/10.1130/0016-7606(2000)112<250:taotdo>2.0.co;2

Baumann, S., Anderson, B., Chinn, T., Mackintosh, A., Collier, C., Lorrey, A. M., et al. (2021). Updated inventory of glacier ice in New Zealand based on 2016 satellite imagery. *Journal of Glaciology*, *67*(261), 13–26. https://doi.org/10.1017/jog.2020.78

Beavan, J., Denys, P., Denham, M., Hager, B., Herring, T., & Molnar, P. (2010). Distribution of present-day vertical deformation across the Southern Alps, New Zealand, from 10 years of GPS data. *Geophysical Research Letters*, *37*(16), L16305. https://doi.org/10.1029/2010gl044165

Ben-Yehoshua, D., Sæmundsson, Þ., Helgason, J. K., Belart, J. M., Sigurðsson, J. V., & Erlingsson, S. (2022). Paraglacial exposure and collapse of glacial sediment: The 2013 landslide onto Svínafellsjökull, southeast Iceland. *Earth Surface Processes and Landforms*, *47*(10), 2612–2627. https://doi.org/10.1002/esp.5398

Beyssac, O., Cox, S., Vry, J., & Herman, F. (2016). Peak metamorphic temperature and thermal history of the Southern Alps (New Zealand). *Tectonophysics*, *676*, 229–249. https://doi.org/10.1016/j.tecto.2015.12.024

Bierman, P., & Steig, E. J. (1996). Estimating rates of denudation using cosmogenic isotope abundances in sediment. *Earth Surface Processes and Landforms*, *21*(2), 125–139. https://doi.org/10.1002/(sici)1096-9837(199602)21:2<125::aid-esp511>3.0.co;2-8

Brozović, N., Burbank, D. W., & Meigs, A. J. (1997). Climatic limits on landscape development in the northwestern Himalaya. *Science*, *276*(5312), 571–574. https://doi.org/10.1126/science.276.5312.571

Burbank, D. W., Leland, J., Fielding, E., Anderson, R. S., Brozovic, N., Reid, M. R., & Duncan, C. (1996). Bedrock incision, rock uplift and threshold hillslopes in the northwestern Himalayas. *Nature*, *379*(6565), 505–510. https://doi.org/10.1038/379505a0

Castelltort, S., Goren, L., Willett, S. D., Champagnac, J. D., Herman, F., & Braun, J. (2012). River drainage patterns in the New Zealand Alps primarily controlled by plate tectonic strain. *Nature Geoscience*, *5*(10), 744–748. https://doi.org/10.1038/ngeo1582

Charreau, J., Blard, P. H., Zumaque, J., Martin, L. C., Delobel, T., & Szafran, L. (2019). Basinga: A cell-by-cell GIS toolbox for computing basin average scaling factors, cosmogenic production rates and denudation rates. *Earth Surface Processes and Landforms*, *44*(12), 2349–2365. https://doi.org/10.1002/esp.4649

Clarke, B. A., & Burbank, D. W. (2010). Bedrock fracturing, threshold hillslopes, and limits to the magnitude of bedrock landslides. *Earth and Planetary Science Letters*, *297*(3), 577–586. https://doi.org/10.1016/j.epsl.2010.07.011

Cody, E., Anderson, B. M., McColl, S. T., Fuller, I. C., & Purdie, H. L. (2020). Paraglacial adjustment of sediment slopes during and immediately after glacial debuttressing. *Geomorphology*, *371*, 107411. https://doi.org/10.1016/j.geomorph.2020.107411

Collins, B. D., & Stock, G. M. (2016). Rockfall triggering by cyclic thermal stressing of exfoliation fractures. *Nature Geoscience*, *9*(5), 395–400. https://doi.org/10.1038/ngeo2686

Cook, S. J., Swift, D. A., Kirkbride, M. P., Knight, P. G., & Waller, R. I. (2020). The empirical basis for modelling glacial erosion rates. *Nature Communications*, *11*(1), 1–7. https://doi.org/10.1038/s41467-020-14583-8

Dadson, S. J., Hovius, N., Chen, H., Dade, W. B., Hsieh, M.-L., Willett, S. D., et al. (2003). Links between erosion, runoff variability and seismicity in the Taiwan orogen. *Nature*, *426*(6967), 648–651. https://doi.org/10.1038/nature02150

Delunel, R., van der Beek, P. A., Carcaillet, J., Bourlès, D. L., & Valla, P. G. (2010). Frost-cracking control on catchment denudation rates: Insights from in situ produced [10]Be concentrations in stream sediments (Ecrins–Pelvoux massif, French Western Alps). *Earth and Planetary Science Letters*, *293*(1–2), 72–83. https://doi.org/10.1016/j.epsl.2010.02.020

DiBiase, R. A. (2018). Increasing vertical attenuation length of cosmogenic nuclide production on steep slopes negates topographic shielding corrections for catchment erosion rates. *Earth Surface Dynamics*, *6*(4), 923–931. https://doi.org/10.5194/esurf-6-923-2018

Draebing, D., & Mayer, T. (2021). Topographic and geologic controls on frost cracking in Alpine rockwalls. *Journal of Geophysical Research: Earth Surface*, *126*(6), e2021JF006163. https://doi.org/10.1029/2021jf006163

Draebing, D., Mayer, T., Jacobs, B., & McColl, S. T. (2022). Alpine rockwall erosion patterns follow elevation-dependent climate trajectories. *Communications Earth & Environment*, *3*(1), 1–12. https://doi.org/10.1038/s43247-022-00348-2

Dymond, J. R., & Shepherd, J. D. (2004a). EcoSat landcover map. 12th of June 2020 Release (version 4) [Dataset]. New Zealand's Landcare Research. https://doi.org/10.26060/01HG-GH20

Dymond, J. R., & Shepherd, J. D. (2004b). The spatial distribution of indigenous forest and its composition in the Wellington region, New Zealand, from ETM+ satellite imagery. *Remote Sensing of Environment*, *90*(1), 116–125. https://doi.org/10.1016/j.rse.2003.11.013

Egholm, D. L., Andersen, J. L., Knudsen, M., Jansen, J. D., & Nielsen, S. (2015). The periglacial engine of mountain erosion—Part 2: Modelling large-scale landscape evolution. *Earth Surface Dynamics*, *3*(4), 463–482. https://doi.org/10.5194/esurf-3-463-2015

Egholm, D. L., Nielsen, S., Pedersen, V., & Lesemann, J.-E. (2009). Glacial effects limiting mountain height. *Nature*, *460*(7257), 884–887. https://doi.org/10.1038/nature08263

Elkadi, J., Lehmann, B., King, G. E., Steinemann, O., Ivy-Ochs, S., Christl, M., & Herman, F. (2022). Quantification of post-glacier bedrock surface erosion in the European Alps using ^{10}Be and optically stimulated luminescence exposure dating. *Earth Surface Dynamics*, *10*(5), 909–928. https://doi.org/10.5194/esurf-10-909-2022

Emberson, R., Hovius, N., Galy, A., & Marc, O. (2016). Chemical weathering in active mountain belts controlled by stochastic bedrock landsliding. *Nature Geoscience*, *9*(1), 42–45. https://doi.org/10.1038/ngeo2600

Forte, A. M., & Whipple, K. X. (2019). The topographic analysis kit (TAK) for TopoToolbox. *Earth Surface Dynamics*, *7*(1), 87–95. https://doi.org/10.5194/esurf-7-87-2019

Geng, H., Hong, Y., Milledge, D. G., Pan, B., & Guo, Y. (2022). Frost cracking dictated landslide distribution in response to temperature change since Last Glacial Maximum across the Eastern Qilian Mountains. *Earth Surface Processes and Landforms*, *47*(13), 3163–3179. https://doi.org/10.1002/esp.5450

GNS Science. (2014). 1:250000 geological map of New Zealand. 2014 release (1st edition) [Dataset]. New Zealand's Institute of Geological and Nuclear Sciences. Retrieved from https://www.gns.cri.nz/data-and-resources/1250-000-geological-map/

Gosse, J. C., Evenson, E. B., Klein, J., Lawn, B., & Middleton, R. (1995). Precise cosmogenic ^{10}Be measurements in western North America: Support for a global Younger Dryas cooling event. *Geology*, *23*(10), 877–880. https://doi.org/10.1130/0091-7613(1995)023<0877:pcbmiw>2.3.co;2

Grämiger, L. M., Moore, J. R., Gischig, V. S., Ivy-Ochs, S., & Loew, S. (2017). Beyond debuttressing: Mechanics of paraglacial rock slope damage during repeat glacial cycles. *Journal of Geophysical Research: Earth Surface*, *122*(4), 1004–1036. https://doi.org/10.1002/2016jf003967

Grämiger, L. M., Moore, J. R., Gischig, V. S., Loew, S., Funk, M., & Limpach, P. (2020). Hydromechanical rock slope damage during Late Pleistocene and Holocene glacial cycles in an Alpine valley. *Journal of Geophysical Research: Earth Surface*, *125*(8), e2019JF005494. https://doi.org/10.1029/2019jf005494

Gruber, S., Hoelzle, M., & Haeberli, W. (2004). Permafrost thaw and destabilization of Alpine rock walls in the hot summer of 2003. *Geophysical Research Letters*, *31*(13). https://doi.org/10.1029/2004gl020051

Hales, T., & Roering, J. J. (2005). Climate-controlled variations in scree production, Southern Alps, New Zealand. *Geology*, *33*(9), 701–704. https://doi.org/10.1130/g21528.1

Hales, T., & Roering, J. J. (2007). Climatic controls on frost cracking and implications for the evolution of bedrock landscapes. *Journal of Geophysical Research*, *112*(F2), F02033. https://doi.org/10.1029/2006jf000616

Hales, T., & Roering, J. J. (2009). A frost "buzzsaw" mechanism for erosion of the eastern Southern Alps, New Zealand. *Geomorphology*, *107*(3–4), 241–253. https://doi.org/10.1016/j.geomorph.2008.12.012

Hartmeyer, I., Delleske, R., Keuschnig, M., Krautblatter, M., Lang, A., Schrott, L., & Otto, J.-C. (2020a). Current glacier recession causes significant rockfall increase: The immediate paraglacial response of deglaciating cirque walls. *Earth Surface Dynamics*, *8*(3), 729–751. https://doi.org/10.5194/esurf-8-729-2020

Hartmeyer, I., Keuschnig, M., Delleske, R., Krautblatter, M., Lang, A., Schrott, L., et al. (2020b). A 6-year lidar survey reveals enhanced rockwall retreat and modified rockfall magnitudes/frequencies in deglaciating cirques. *Earth Surface Dynamics*, *8*(3), 753–768. https://doi.org/10.5194/esurf-8-753-2020

Herman, F., Beyssac, O., Brughelli, M., Lane, S. N., Leprince, S., Adatte, T., et al. (2015). Erosion by an alpine glacier. *Science*, *350*(6257), 193–195. https://doi.org/10.1126/science.aab2386

Herman, F., Cox, S. C., & Kamp, P. J. (2009). Low-temperature thermochronology and thermokinematic modeling of deformation, exhumation, and development of topography in the central Southern Alps, New Zealand. *Tectonics*, *28*(5), TC5011. https://doi.org/10.1029/2008tc002367

Heron, D. W. (2014). *Geological map of New Zealand 1: 250 000: Digital vector data 2014*. GNS Science.

Hicks, D. M., Shankar, U., McKerchar, A. I., Basher, L., Lynn, I., Page, M., & Jessen, M. (2011). Suspended sediment yields from New Zealand rivers. *Journal of Hydrology*, 81–142.

Hovius, N., Stark, C. P., & Allen, P. A. (1997). Sediment flux from a mountain belt derived by landslide mapping. *Geology*, *25*(3), 231–234. https://doi.org/10.1130/0091-7613(1997)025<0231:sffamb>2.3.co;2

Howarth, J. D., Fitzsimons, S. J., Norris, R. J., & Jacobsen, G. E. (2014). Lake sediments record high intensity shaking that provides insight into the location and rupture length of large earthquakes on the Alpine Fault, New Zealand. *Earth and Planetary Science Letters*, *403*, 340–351. https://doi.org/10.1016/j.epsl.2014.07.008

Hugentobler, M., Aaron, J., Loew, S., & Roques, C. (2022). Hydro-mechanical interactions of a rock slope with a retreating temperate valley glacier. *Journal of Geophysical Research: Earth Surface*, *127*(4), e2021JF006484. https://doi.org/10.1029/2021jf006484

Jiao, R., Herman, F., Beyssac, O., Adatte, T., Cox, S. C., Nelson, F. E., & Neil, H. L. (2018). Erosion of the southern alps of New Zealand during the last deglaciation. *Geology*, *46*(11), 975–978. https://doi.org/10.1130/g45160.1

Kamb, B. (1970). Sliding motion of glaciers: Theory and observation. *Reviews of Geophysics*, *8*(4), 673–728. https://doi.org/10.1029/rg008i004p00673

Kaplan, M. R., Schaefer, J. M., Denton, G. H., Doughty, A. M., Barrell, D. J., Chinn, T. J., et al. (2013). The anatomy of long-term warming since 15 ka in New Zealand based on net glacier snowline rise. *Geology*, *41*(8), 887–890. https://doi.org/10.1130/g34288.1

Koppes, M., Hallet, B., Rignot, E., Mouginot, J., Wellner, J. S., & Boldt, K. (2015). Observed latitudinal variations in erosion as a function of glacier dynamics. *Nature*, *526*(7571), 100–103. https://doi.org/10.1038/nature15385

LaHusen, S. R., Duvall, A. R., Booth, A. M., Grant, A., Mishkin, B. A., Montgomery, D. R., et al. (2020). Rainfall triggers more deep-seated landslides than Cascadia earthquakes in the Oregon Coast Range, USA. *Science Advances*, *6*(38), eaba6790. https://doi.org/10.1126/sciadv.aba6790

Lal, D. (1991). Cosmic ray labeling of erosion surfaces: In situ nuclide production rates and erosion models. *Earth and Planetary Science Letters*, *104*(2–4), 424–439. https://doi.org/10.1016/0012-821X(91)90220-C

Langridge, R., Ries, W., Dolan, J., Schermer, E., & Siddoway, C. (2017). Slip rate estimates and slip gradient for the Alpine Fault at calf paddock, Maruia River, New Zealand. *New Zealand Journal of Geology and Geophysics*, *60*(2), 73–88. https://doi.org/10.1080/00288306.2016.1275707

Langridge, R., Villamor, P., Basili, R., Almond, P., Martinez-Diaz, J., & Canora, C. (2010). Revised slip rates for the Alpine fault at Inchbonnie: Implications for plate boundary kinematics of South Island, New Zealand. *Lithosphere*, *2*(3), 139–152. https://doi.org/10.1130/l88.1

Larsen, I. J., Almond, P. C., Eger, A., Stone, J. O., Montgomery, D. R., & Malcolm, B. (2014). Rapid soil production and weathering in the Southern Alps, New Zealand. *Science*, *343*(6171), 637–640. https://doi.org/10.1126/science.1244908

Larsen, I. J., Eger, A., Almond, P. C., Thaler, E. A., Rhodes, J. M., & Prasicek, G. (2023). The influence of erosion and vegetation on soil production and chemical weathering rates in the Southern Alps, New Zealand. *Earth and Planetary Science Letters*, *608*, 118036. https://doi.org/10.1016/j.epsl.2023.118036

Larsen, I. J., & Montgomery, D. R. (2012). Landslide erosion coupled to tectonics and river incision. *Nature Geoscience*, *5*(7), 468–473. https://doi.org/10.1038/ngeo1479

Larsen, I. J., Montgomery, D. R., & Korup, O. (2010). Landslide erosion controlled by hillslope material. *Nature Geoscience*, *3*(4), 247–251. https://doi.org/10.1038/ngeo776

Lehmann, B., Herman, F., Valla, P. G., King, G. E., Biswas, R. H., Ivy-Ochs, S., et al. (2020). Postglacial erosion of bedrock surfaces and deglaciation timing: New insights from the Mont Blanc massif (western Alps). *Geology*, *48*(2), 139–144. https://doi.org/10.1130/g46585.1

Little, T. A., Cox, S., Vry, J. K., & Batt, G. (2005). Variations in exhumation level and uplift rate along the oblique-slip Alpine fault, central Southern Alps, New Zealand. *GSA Bulletin*, *117*(5–6), 707–723. https://doi.org/10.1130/b25500.1

Lorrey, A. M., Vargo, L., Purdie, H., Anderson, B., Cullen, N. J., Sirguey, P., et al. (2022). Southern alps equilibrium line altitudes: Four decades of observations show coherent glacier–climate responses and a rising snowline trend. *Journal of Glaciology*, *68*(272), 1–14. https://doi.org/10.1017/jog.2022.27

Marc, O., Behling, R., Andermann, C., Turowski, J. M., Illien, L., Roessner, S., & Hovius, N. (2019). Long-term erosion of the Nepal Himalayas by bedrock landsliding: The role of monsoons, earthquakes and giant landslides. *Earth Surface Dynamics*, *7*(1), 107–128. https://doi.org/10.5194/esurf-7-107-2019

Marc, O., Stumpf, A., Malet, J.-P., Gosset, M., Uchida, T., & Chiang, S.-H. (2018). Initial insights from a global database of rainfall-induced landslide inventories: The weak influence of slope and strong influence of total storm rainfall. *Earth Surface Dynamics*, *6*(4), 903–922. https://doi.org/10.5194/esurf-6-903-2018

Marshall, J. A., Roering, J., Rempel, A., Shafer, S., & Bartlein, P. (2021). Extensive frost weathering across unglaciated North America during the Last glacial maximum. *Geophysical Research Letters*, *48*(5), e2020GL090305. https://doi.org/10.1029/2020gl090305

Marshall, J. A., Roering, J. J., Bartlein, P. J., Gavin, D. G., Granger, D. E., Rempel, A. W., et al. (2015). Frost for the trees: Did climate increase erosion in unglaciated landscapes during the late Pleistocene? *Science Advances*, *1*(10), e1500715. https://doi.org/10.1126/sciadv.1500715

McKinzey, K. M., Lawson, W., Kelly, D., & Hubbard, A. (2004). A revised Little ice age chronology of the Franz Josef glacier, Westland, New Zealand. *Journal of the Royal Society of New Zealand*, *34*(4), 381–394. https://doi.org/10.1080/03014223.2004.9517774

Moon, S., Page Chamberlain, C., Blisniuk, K., Levine, N., Rood, D. H., & Hilley, G. E. (2011). Climatic control of denudation in the deglaciated landscape of the Washington Cascades. *Nature Geoscience*, *4*(7), 469–473. https://doi.org/10.1038/ngeo1159

Nibourel, L., Herman, F., Cox, S. C., Beyssac, O., & Lavé, J. (2015). Provenance analysis using Raman spectroscopy of carbonaceous material: A case study in the southern alps of New Zealand. *Journal of Geophysical Research: Earth Surface*, *120*(10), 2056–2079. https://doi.org/10.1002/2015jf003541

Niemi, N. A., Oskin, M., Burbank, D. W., Heimsath, A. M., & Gabet, E. J. (2005). Effects of bedrock landslides on cosmogenically determined erosion rates. *Earth and Planetary Science Letters*, *237*(3), 480–498. https://doi.org/10.1016/j.epsl.2005.07.009

Nishiizumi, K., Winterer, E., Kohl, C., Klein, J., Middleton, R., Lal, D., & Arnold, J. (1989). Cosmic ray production rates of [10]Be and [26]Al in quartz from glacially polished rocks. *Journal of Geophysical Research*, *94*(B12), 17907–17915. https://doi.org/10.1029/jb094ib12p17907

Noetzli, J., Hoelzle, M., & Haeberli, W. (2003). Mountain permafrost and recent alpine rock-fall events: A GIS-based approach to determine critical factors. In *Proceedings of the 8th international conference on permafrost*.

Norris, R. J., & Cooper, A. F. (2001). Late Quaternary slip rates and slip partitioning on the Alpine Fault, New Zealand. *Journal of Structural Geology*, *23*(2–3), 507–520. https://doi.org/10.1016/s0191-8141(00)00122-x

Pedersen, V., Egholm, D., & Nielsen, S. (2010). Alpine glacial topography and the rate of rock column uplift: A global perspective. *Geomorphology*, *122*(1–2), 129–139. https://doi.org/10.1016/j.geomorph.2010.06.005

Prasicek, G., Larsen, I. J., & Montgomery, D. R. (2015). Tectonic control on the persistence of glacially sculpted topography. *Nature Communications*, *6*(1), 1–6. https://doi.org/10.1038/ncomms9028

Putnam, A. E., Schaefer, J., Barrell, D., Vandergoes, M., Denton, G., Kaplan, M., et al. (2010). In situ cosmogenic [10]Be production-rate calibration from the Southern Alps, New Zealand. *Quaternary Geochronology*, *5*(4), 392–409. https://doi.org/10.1016/j.quageo.2009.12.001

Putnam, A. E., Schaefer, J. M., Denton, G. H., Barrell, D. J., Finkel, R. C., Andersen, B. G., et al. (2012). Regional climate control of glaciers in New Zealand and Europe during the pre-industrial Holocene. *Nature Geoscience*, *5*(9), 627–630. https://doi.org/10.1038/ngeo1548

Ravanel, L., & Deline, P. (2011). Climate influence on rockfalls in high-Alpine steep rockwalls: The north side of the Aiguilles de Chamonix (Mont Blanc massif) since the end of the 'Little Ice Age'. *The Holocene*, *21*(2), 357–365. https://doi.org/10.1177/0959683610374887

Rempel, A. W., Marshall, J. A., & Roering, J. J. (2016). Modeling relative frost weathering rates at geomorphic scales. *Earth and Planetary Science Letters*, *453*, 87–95. https://doi.org/10.1016/j.epsl.2016.08.019

Rengers, F. K., Kean, J. W., Reitman, N. G., Smith, J. B., Coe, J. A., & McGuire, L. A. (2020). The influence of frost weathering on debris flow sediment supply in an alpine basin. *Journal of Geophysical Research: Earth Surface*, *125*(2), e2019JF005369. https://doi.org/10.1029/2019jf005369

Robinson, T., Davies, T., Wilson, T., & Orchiston, C. (2016). Coseismic landsliding estimates for an Alpine Fault earthquake and the consequences for erosion of the Southern Alps, New Zealand. *Geomorphology*, *263*, 71–86. https://doi.org/10.1016/j.geomorph.2016.03.033

Roda-Boluda, D. C. (2023). Supplementary files for the manuscript "Elevation-dependent periglacial and paraglacial processes modulate tectonically-controlled erosion of the Western Southern Alps, New Zealand", submitted to JGR Earth Surface (Version 1) [Dataset]. Zenodo. https://doi.org/10.5281/zenodo.8385574

Roda-Boluda, D. C., D'Arcy, M., Whittaker, A. C., Gheorghiu, D. M., & Rodés, Á. (2019). [10]Be erosion rates controlled by transient response to normal faulting through incision and landsliding. *Earth and Planetary Science Letters*, *507*, 140–153. https://doi.org/10.1016/j.epsl.2018.11.032

Roe, G. H., Montgomery, D. R., & Hallet, B. (2003). Orographic precipitation and the relief of mountain ranges. *Journal of Geophysical Research*, *108*(B6), 2315. https://doi.org/10.1029/2001jb001521

Sattler, K., Anderson, B., Mackintosh, A., Norton, K., & de Róiste, M. (2016). Estimating permafrost distribution in the maritime Southern Alps, New Zealand, based on climatic conditions at rock glacier sites. *Frontiers in Earth Science*, *4*, 4. https://doi.org/10.3389/feart.2016.00004

Savi, S., Delunel, R., & Schlunegger, F. (2015). Efficiency of frost-cracking processes through space and time: An example from the eastern Italian Alps. *Geomorphology*, *232*, 248–260. https://doi.org/10.1016/j.geomorph.2015.01.009

Schaefer, J. M., Codilean, A. T., Willenbring, J. K., Lu, Z.-T., Keisling, B., Fülöp, R.-H., & Val, P. (2022). Cosmogenic nuclide techniques. *Nature Reviews Methods Primers*, *2*(1), 1–22. https://doi.org/10.1038/s43586-022-00096-9

Schildgen, T. F., Phillips, W., & Purves, R. (2005). Simulation of snow shielding corrections for cosmogenic nuclide surface exposure studies. *Geomorphology*, *64*(1–2), 67–85. https://doi.org/10.1016/j.geomorph.2004.05.003

Schildgen, T. F., van der Beek, P. A., D'Arcy, M., Roda-Boluda, D., Orr, E. N., & Wittmann, H. (2022). Quantifying drainage-divide migration from orographic rainfall over geologic timescales: Sierra de Aconquija, southern Central Andes. *Earth and Planetary Science Letters*, *579*, 117345. https://doi.org/10.1016/j.epsl.2021.117345

Schwanghart, W., & Scherler, D. (2014). TopoToolbox 2–MATLAB-based software for topographic analysis and modeling in Earth surface sciences. *Earth Surface Dynamics*, *2*(1), 1–7. https://doi.org/10.5194/esurf-2-1-2014

Shankar, U., & Hicks, D. M. (2002). Suspended-sediment yield estimator. November 29, 2002 Release [Dataset]. New Zealand's National Institute of Water and Atmospheric Research (NIWA). Retrieved from https://niwa.co.nz/freshwater/management-tools/sediment-tools/suspended-sediment-yield-estimator

Sklar, L. S., Riebe, C. S., Marshall, J. A., Genetti, J., Leclere, S., Lukens, C. L., & Merces, V. (2017). The problem of predicting the size distribution of sediment supplied by hillslopes to rivers. *Geomorphology*, *277*, 31–49. https://doi.org/10.1016/j.geomorph.2016.05.005

Tait, A., & Macara, G. (2014). Evaluation of interpolated daily temperature data for high elevation areas in New Zealand. *Weather and Climate*, *34*, 36–49. https://doi.org/10.2307/26169743

Tait, A., Sturman, J., & Clark, M. (2012). An assessment of the accuracy of interpolated daily rainfall for New Zealand. *Journal of Hydrology*, 25–44.

Tait, A., & Zheng, X. (2007). National and regional climate maps. May 2007 Release [Dataset]. New Zealand's National Institute of Water and Atmospheric Research (NIWA). Retrieved from https://niwa.co.nz/climate/research-projects/national-and-regional-climate-maps

Tielidze, L. G., Eaves, S. R., Norton, K. P., Mackintosh, A. N., & Hidy, A. J. (2022). Cosmogenic ^{10}Be constraints on deglacial snowline rise in the Southern Alps, New Zealand. *Quaternary Science Reviews*, *286*, 107548. https://doi.org/10.1016/j.quascirev.2022.107548

Tippett, J. M., & Kamp, P. J. J. (1993a). Fission track analysis of the Late Cenozoic vertical kinematics of continental pacific crust, South Island, New Zealand. *Journal of Geophysical Research*, *98*(B9), 16119–16148. https://doi.org/10.1029/92JB02115

Tippett, J. M., & Kamp, P. J. J. (1993b). The role of faulting in rock uplift in the Southern Alps, New Zealand. *New Zealand Journal of Geology and Geophysics*, *36*(4), 497–504. https://doi.org/10.1080/00288306.1993.9514595

van der Beek, P., & Schildgen, T. F. (2023). age2exhume—A MATLAB/Python script to calculate steady-state vertical exhumation rates from thermochronometric ages and application to the Himalaya. *Geochronology*, *5*(1), 35–49. https://doi.org/10.5194/gchron-5-35-2023

Van Zyl, J. J. (2001). The Shuttle Radar Topography Mission (SRTM): A breakthrough in remote sensing of topography. *Acta Astronautica*, *48*(5–12), 559–565. https://doi.org/10.1016/s0094-5765(01)00020-0

von Blanckenburg, F. (2005). The control mechanisms of erosion and weathering at basin scale from cosmogenic nuclides in river sediment. *Earth and Planetary Science Letters*, *237*(3–4), 462–479. https://doi.org/10.1016/j.epsl.2005.06.030

Von Blanckenburg, F., Hewawasam, T., & Kubik, P. W. (2004). Cosmogenic nuclide evidence for low weathering and denudation in the wet, tropical highlands of Sri Lanka. *Journal of Geophysical Research*, *109*(F3), F03008. https://doi.org/10.1029/2003jf000049

Walder, J., & Hallet, B. (1985). A theoretical model of the fracture of rock during freezing. *Geological Society of America Bulletin*, *96*(3), 336–346. https://doi.org/10.1130/0016-7606(1985)96<336:atmotf>2.0.co;2

Wang, J., Howarth, J. D., McClymont, E. L., Densmore, A. L., Fitzsimons, S. J., Croissant, T., et al. (2020). Long-term patterns of hillslope erosion by earthquake-induced landslides shape mountain landscapes. *Science Advances*, *6*(23), eaaz6446. https://doi.org/10.1126/sciadv.aaz6446

Whipple, K. X. (2009). The influence of climate on the tectonic evolution of mountain belts. *Nature Geoscience*, *2*(2), 97–104. https://doi.org/10.1038/ngeo413

Whipple, K. X., Kirby, E., & Brocklehurst, S. H. (1999). Geomorphic limits to climate-induced increases in topographic relief. *Nature*, *401*(6748), 39–43. https://doi.org/10.1038/43375

Willett, S. D., & Brandon, M. T. (2002). On steady states in mountain belts. *Geology*, *30*(2), 175–178. https://doi.org/10.1130/0091-7613(2002)030<0175:ossimb>2.0.co;2

Willett, S. D., & Brandon, M. T. (2013). Some analytical methods for converting thermochronometric age to erosion rate. *Geochemistry, Geophysics, Geosystems*, *14*(1), 209–222. https://doi.org/10.1029/2012gc004279

Williams, H. B., & Koppes, M. N. (2019). A comparison of glacial and paraglacial denudation responses to rapid glacial retreat. *Annals of Glaciology*, *60*(80), 151–164. https://doi.org/10.1017/aog.2020.1

Winkler, S. (2000). The 'Little ice Age' maximum in the southern alps, New Zealand: Preliminary results at Mueller glacier. *The Holocene*, *10*(5), 643–647. https://doi.org/10.1191/095968300666087656

Wittmann, H., Malusà, M. G., Resentini, A., Garzanti, E., & Niedermann, S. (2016). The cosmogenic record of mountain erosion transmitted across a foreland basin: Source-to-sink analysis of in situ ^{10}Be, ^{26}Al and ^{21}Ne in sediment of the Po river catchment. *Earth and Planetary Science Letters*, *452*, 258–271. https://doi.org/10.1016/j.epsl.2016.07.017

Wittmann, H., von Blanckenburg, F., Kruesmann, T., Norton, K. P., & Kubik, P. W. (2007). Relation between rock uplift and denudation from cosmogenic nuclides in river sediment in the Central Alps of Switzerland. *Journal of Geophysical Research*, *112*(F4), F04010. https://doi.org/10.1029/2006jf000729

Yanites, B. J., Tucker, G. E., & Anderson, R. S. (2009). Numerical and analytical models of cosmogenic radionuclide dynamics in landslide-dominated drainage basins. *Journal of Geophysical Research*, *114*(F1), F01007. https://doi.org/10.1029/2008jf001088

References From the Supporting Information

Balco, G. (2006). Converting Al and Be isotope ratio measurements to nuclide concentrations in quartz. In *Documentation—Be-10/26-Al exposure age calculator*.

Batt, G. E., Baldwin, S. L., Cottam, M. A., Fitzgerald, P. G., Brandon, M. T., & Spell, T. L. (2004). Cenozoic plate boundary evolution in the South Island of New Zealand: New thermochronological constraints. *Tectonics*, *23*(4), TC4001. https://doi.org/10.1029/2003tc001527

Batt, G. E., Kohn, B. P., Braun, J., McDougall, I., & Ireland, T. R. (1999). New insight into the dynamic development of the Southern Alps, New Zealand, from detailed thermochronological investigation of the Mataketake Range pegmatites. *Geological Society, London, Special Publications*, *154*(1), 261–282. https://doi.org/10.1144/gsl.sp.1999.154.01.12

Gregorich, M., Strohmaier, S., Dunkler, D., & Heinze, G. (2021). Regression with highly correlated predictors: Variable omission is not the solution. *International Journal of Environmental Research and Public Health*, *18*(8), 4259. https://doi.org/10.3390/ijerph18084259

Herman, F., Braun, J., & Dunlap, W. J. (2007). Tectonomorphic scenarios in the Southern alps of New Zealand. *Journal of Geophysical Research*, *112*(B4), B04201. https://doi.org/10.1029/2004jb003472

Johnston, R., Jones, K., & Manley, D. (2018). Confounding and collinearity in regression analysis: A cautionary tale and an alternative procedure, illustrated by studies of British voting behaviour. *Quality and Quantity*, *52*(4), 1957–1976. https://doi.org/10.1007/s11135-017-0584-6

Kamp, P. J., Green, P. F., & Tippett, J. M. (1992). Tectonic architecture of the mountain front-foreland basin transition, South Island, New Zealand, assessed by fission track analysis. *Tectonics*, *11*(1), 98–113. https://doi.org/10.1029/91tc02362

Kamp, P. J., Green, P. F., & White, S. H. (1989). Fission track analysis reveals character of collisional tectonics in New Zealand. *Tectonics*, *8*(2), 169–195. https://doi.org/10.1029/tc008i002p00169

Kao, M.-H. (2001). Thermo-tectonic history of the Marlborough region, South Island, New Zealand. *Terrestrial, Atmospheric and Oceanic Sciences*, *12*(3), 485–502. https://doi.org/10.3319/tao.2001.12.3.485(t)

Mifsud, C., Fujioka, T., & Fink, D. (2013). Extraction and purification of quartz in rock using hot phosphoric acid for in situ cosmogenic exposure dating. *Nuclear Instruments and Methods in Physics Research Section B: Beam Interactions with Materials and Atoms*, *294*, 203–207. https://doi.org/10.1016/j.nimb.2012.08.037

Nishiizumi, K., Imamura, M., Caffee, M. W., Southon, J. R., Finkel, R. C., & McAninch, J. (2007). Absolute calibration of ^{10}Be AMS standards. *Nuclear Instruments and Methods in Physics Research Section B: Beam Interactions with Materials and Atoms*, *258*(2), 403–413. https://doi.org/10.1016/j.nimb.2007.01.297

Ring, U., & Bernet, M. (2010). Fission-track analysis unravels the denudation history of the Bonar range in the footwall of the Alpine Fault, South Island, New Zealand. *Geological Magazine*, *147*(6), 801–813. https://doi.org/10.1017/s0016756810000208

Seward, D., & Nathan, S. (1990). Uplift history of South Westland using the fission-track dating technique. *New Zealand Journal of Geology and Geophysics*, *33*(2), 201–204. https://doi.org/10.1080/00288306.1990.10425678

Seward, D., & Tulloch, A. (1991). Fission-track analysis of tertiary uplift history of granitic basement in the Victoria Range, West Coast, New Zealand. *New Zealand Journal of Geology and Geophysics*, *34*(2), 115–120. https://doi.org/10.1080/00288306.1991.9514448

Sutherland, R., Gurnis, M., Kamp, P. J., & House, M. A. (2009). Regional exhumation history of brittle crust during subduction initiation, Fiordland, southwest New Zealand, and implications for thermochronologic sampling and analysis strategies. *Geosphere*, *5*(5), 409–425. https://doi.org/10.1130/ges00225.sa2

White, S., & Green, P. (1986). Tectonic development of the Alpine Fault zone, New Zealand: A fission-track study. *Geology*, *14*(2), 124–127. https://doi.org/10.1130/0091-7613(1986)14<124:tdotaf>2.0.co;2